

2

SECURITY

AD-A201 442

DOCUMENTATION PAGE

1a. REPORT UNCLASSIFIED			1b. RESTRICTIVE MARKINGS DTIC FILE COPY														
2a. DECLASSIFICATION/DOWNGRADING SCHEDULE SELECTED DEC 15 1988			3. DISTRIBUTION/AVAILABILITY OF REPORT Approved for public release; distribution unlimited.														
4. PERFORMING ORGANIZATION REPORT NUMBER(S) D CB			5. MONITORING ORGANIZATION REPORT NUMBER(S) AFOSR-TK- 88-1321														
6a. NAME OF PERFORMING ORGANIZATION Cornell University		6b. OFFICE SYMBOL (If applicable)	7a. NAME OF MONITORING ORGANIZATION AFOSR/NE														
6c. ADDRESS (City, State and ZIP Code) School of Applied & Engineering Physics Ithaca, NY 14853			7b. ADDRESS (City, State and ZIP Code) Bldg 410 Bolling AFB DC 20332-6448														
8a. NAME OF FUNDING/SPONSORING ORGANIZATION AFOSR/NE		8b. OFFICE SYMBOL (If applicable) NE	9. PROCUREMENT INSTRUMENT IDENTIFICATION NUMBER AFOSR 84 0314														
8c. ADDRESS (City, State and ZIP Code) Bldg 410 Bolling AFB DC 20332-6448			10. SOURCE OF FUNDING NOS. <table border="1"><tr><td>PROGRAM ELEMENT NO. 61102F</td><td>PROJECT NO. 2306</td><td>TASK NO. B1</td><td>WORK UNIT NO.</td></tr></table>			PROGRAM ELEMENT NO. 61102F	PROJECT NO. 2306	TASK NO. B1	WORK UNIT NO.								
PROGRAM ELEMENT NO. 61102F	PROJECT NO. 2306	TASK NO. B1	WORK UNIT NO.														
11. TITLE (Include Security Classification) Wavelength Independent Optical Microscopy & Lithography																	
12. PERSONAL AUTHOR(S) Lewis																	
13a. TYPE OF REPORT Final		13b. TIME COVERED FROM 01Sep84 TO 31Aug87		14. DATE OF REPORT (Yr., Mo., Day)													
15. PAGE COUNT																	
16. SUPPLEMENTARY NOTATION																	
17. COSATI CODES <table border="1"><tr><td>FIELD</td><td>GROUP</td><td>SUB. GR.</td></tr><tr><td></td><td></td><td></td></tr><tr><td></td><td></td><td></td></tr><tr><td></td><td></td><td></td></tr></table>			FIELD	GROUP	SUB. GR.										18. SUBJECT TERMS (Continue on reverse if necessary and identify by block number)		
FIELD	GROUP	SUB. GR.															
19. ABSTRACT (Continue on reverse if necessary and identify by block number) <p>At the start of the present contract we had only a rudimentary understanding of the nature of the near-field. As a result of this contract, great progress has been made both in building a theoretical foundation and underpinning this foundation with crucial experiments. The fundamental principle underlying the NSOM concept is outlined in Figure 1, where visible light is depicted as being normally incident on a conducting screen containing a small (sub-wavelength) aperture. Because the screen is completely opaque, the radiation emanating through the aperture and into the region beyond the screen is first collimated to the aperture size rather than to the wavelength of the radiation employed.</p> <p style="text-align: right;">(signature) ←</p> <p style="text-align: right;">8 1 20</p>																	
20. DISTRIBUTION/AVAILABILITY OF ABSTRACT UNCLASSIFIED/UNLIMITED <input type="checkbox"/> SAME AS RPT. <input type="checkbox"/> DTIC USERS <input type="checkbox"/>			21. ABSTRACT SECURITY CLASSIFICATION UNCLASSIFIED														
22a. NAME OF RESPONSIBLE INDIVIDUAL Malloy		22b. TELEPHONE NUMBER (Include Area Code) (202) 767-4931		22c. OFFICE SYMBOL NE													

AFOUR-TR. 88-1321

FINAL TECHNICAL REPORT

on

**Wavelength Independent Optical Microscopy
and Lithography [Grant #AFOSR-84-0314]**

Submitted by:

M. Isaacson and A. Lewis
Cornell University
School of Applied and Engineering Physics
Clark Hall
Ithaca, New York 14853

Submitted to:

United States Air Force
Office of Scientific Research

October 31, 1987

[illegible]

INSPIRATION

FINAL REPORT

With the help of the Air Force we have been able to develop a new area of optics which is based on the collimation of near-field radiation. The near-field allows super spatial resolution for the characterization and fabrication of materials.

CONCEPTUAL BASIS OF NEAR-FIELD SCANNING OPTICAL MICROSCOPY

At the start of the present contract we had only a rudimentary understanding of the nature of the near-field. As a result of this contract, great progress has been made both in building a theoretical foundation and underpinning this foundation with crucial experiments. The fundamental principle underlying the NSOM concept is outlined in Figure 1, where visible light is depicted as being normally incident on a conducting screen containing a small (sub-wavelength) aperture. Because the screen is completely opaque, the radiation emanating through the aperture and into the region beyond the screen is first collimated to the aperture size rather than to the wavelength of the radiation employed. This occurs in the near-field regime. Eventually the effect of diffraction is evidenced as a marked divergence in the radiation, resulting in a pattern that no longer reproduces the geometrical image of the aperture. This occurs in the far-field regime.

To apply the collimation phenomena, an object, such as an integrated circuit, is placed within the near-field region relative to an aperture. In this case, the aperture acts as a light source whose size is not limited by the considerations of geometrical optics. The light source can be scanned relative to the object, and the detected light can be used to generate a high-resolution image. Because the resolution is dependent upon the aperture size rather than the wavelength, it is possible to obtain resolution of $<50\text{nm}$, which is comparable to scanning electron microscopes, if sufficiently small apertures are used. These are the essential features of the NSOM technique, which, unlike electron microscopic methods, can be applied in air using non-ionizing visible radiation and can form images of fluorescing objects with this same degree of super-resolution.

HISTORICAL BACKGROUND

As far back as a decade ago, the principle of super-resolution microscopy was demonstrated at microwave frequencies using a wavelength of 3cm by Ash and Nicholls (1). In their pioneering experiment, a grating of 0.5mm periodicity was imaged with an effective resolution of $1/60$ the wavelength. However, until we reported our initial results in 1984 (2), there were no published attempts to extend this technique to the visible region of the spectrum. This is quite understandable, because the minute physical dimensions of the optical near-field demand aperture fabrication and micropositioning technologies on a nanometer scale. Furthermore, it is not immediately obvious that the results of the microwave experiment could be extended to the visible regime, because in the optical regime, thin metal films with finite conductivity had to be used to construct subwavelength apertures whereas in the microwave case comparatively thicker metal screens with infinite conductivity could be used. These questions together with the inability of the microwave microscope to scan rough surfaces led to little interest in the field.

However, since our original reports (2), several additional publications in the area of near-field imaging have appeared. Fischer (3) in West Germany has produced an interesting series of results by scanning a subwavelength aperture over a second, larger aperture, but these results were difficult to interpret for a number of reasons. For example, the opacity of the metal film used was not large so that the aperture was poorly defined and much stray light was transmitted through the aperture screens. In addition, because of the grazing incidence illumination in his experiment, a series of standing waves were generated when the polarization of the electric field was perpendicular to these screens.

Durig, et al. (4) in Zurich produced apertures at the tip of a single crystal of quartz etched using HF to make a fine point and covered this by metal. These apertures were difficult to produce reproducibly and to characterize because they were manufactured by thrusting this metal covered pyramidal quartz crystal against glass slide and detecting the first instant when light emanated from the aperture. Furthermore, these workers had difficulty in making test structures to demonstrate $<50\text{nm}$ resolution. With any new form of microscopy it is essential to have test structures well-characterized by an established technique in order to verify the claim of subwavelength capability.

In short, initial attempts to implement the near-field scanning concept attest to the difficulty of the NSOM technique. To appreciate the technical challenges inherent in this form of microscopy, we completed detailed calculations under this contract to obtain a first approximation for how the radiation spreads out as it emanates from a subwavelength aperture. These calculations (5) and others completed on this contract (6,7) investigate the transmission of light through slits and apertures in screens of finite thickness.

In particular, the component of the time-averaged Poynting vector perpendicular to the screen was calculated in the region just beyond the screen. The results are shown in Figure 2, where the divergence of the energy flux is plotted as a function of the distance from the aperture. These results indicate that the radiation remains collimated to a distance of approximately the aperture diameter. Finally, the near-field energy flux calculations exhibit a close-to-exponential decrease in intensity with increasing distance from the screen. This suggests that rigid stability requirements are required for the z direction even for rough surfaces.

OVERCOMING THE TECHNICAL CHALLENGES

Aperture Fabrication

Several different methods have been used in the past to fabricate the submicron apertures needed in near-field microscopy (2-4). However, under this contract we developed an inexpensive, rapid, and highly reproducible method for producing such apertures at the tips of metallized glass pipettes. Besides the ease, rapidity, cheapness and reproducibility of our new technique an important advantage of our method is that these apertures at the tip of highly tapered pipettes can probe even recessed regions of rough surfaces. To form such apertures with diameters ranging from 50nm to 1000nm from glass micropipettes a two stage pulling process was used. Scanning electron

micrographs of a 100nm diameter pipette and a 500nm diameter pipette are compared in Figure 3. These pipettes were metallized with 8nm of chromium followed by 50nm of aluminum. The chromium was used as an adhesive layer between the glass pipette and the 50nm aluminum layer. Aluminum was chosen for its high absorption coefficient at optical wavelengths.

Our early attempts at forming these pipette apertures produced tip outer diameters of approximately 500nm for the smaller aperture pipettes. However, recently we have produced tips with outer diameters of 60nm, see Figure 4, using techniques used by biologists to produce pipettes for the microinjection of individual cells (8). We have discovered that we can make even smaller diameter pipettes with apertures at the tips by using aluminumsilicate instead of borosilicate glass. And we are now trying to optimize this new form of light wave technology.

Our application of these pipette type apertures to near-field microscopy and our demonstration (9) of large light throughputs from such apertures has resolved one of the principal problems in scanning rough, real surfaces with this form of super-resolution microscopy.

Micropositioning

Another major problem overcome during this contract year has been the development of a methodology to position an aperture 50nm above a surface with the 3nm accuracy required by the exponential behavior of the near-field. The placement of the aperture at the tip of a pipette certainly simplifies the problem but there has to be a feedback mechanism that will allow for the accurate positioning of the aperture above the surface. We have developed three distinct solutions to this problem all of which work well at resolving this potential barrier to near-field microscopy.

One method for distance regulation is based on an exquisitely sensitive technique for monitoring z topography developed by Matey and Blanc (10). In this technique the sample and a probe tip form a capacitor and changes in separation between the sample and the probe result in changes in capacitance. The capacitance changes can be detected with a high Q RLC circuit. We have modified the technique in two ways. First, we employ our metal coated pipette aperture instead of the stylus probe of an RCA videoplayer used by these previous workers. Second, position modulation of the probe is used. Thus we have incorporated essentially an electrical heterodyning method. With this modulation the detected signal has components at different frequencies and this permits the decoupling of the dielectric information from the topographic information. With such position modulation the technique should be sensitive to changes of less than 10^{-16} farads. The advantages of this technique for z position regulation in near-field microscopy are three fold. First, because of its sensitivity, the capacitive method can respond quickly even to very small topographical changes and this allows for rapid (kHz) near-field scanning. Second, with position modulation it is possible to generate a signal which depends solely on topography and not on material properties (i.e. dielectric properties) of the surface. Third, for the probe size that we use, the capacitance changes can be detected from as far as 50nm from the surface.

In the eventuality that the sample is not conducting the light emanating from a subwavelength aperture in an opaque screen decreases exponentially with distance from the screen (5). Hence, in a reflection mode, the intensity of the light reflected back through the aperture is strongly dependent upon the aperture-sample separation and can be used to form a distance regulation system. In this method position modulation can also be employed to extract topographical information.

Finally, Durig, et al. (4) have employed the new methodology of tunneling microscopy (11) to accurately measure the z position of the aperture. However with tunneling microscopy the probe has to approach within 2 nm of the surface and this is at least an order of magnitude closer than is required for NSOM.

Vibration, acoustic and thermal isolation

In a typical laboratory environment, building vibrations exist at frequencies as low as 2-4Hz, although most of the vibrational energy is in the 5-30Hz range (12). In our environment, we have measured displacements of up to one micron in this frequency range. If this energy were to be transferred without attenuation to the critical components of an NSOM system, and if the aperture and object were not held together with sufficient rigidity, then their relative displacement could vary by two to three orders of magnitude greater than the precision required. To preclude this possibility, it is necessary to design an isolation system which attenuates both horizontal and vertical vibrations from the floor at frequencies above a few hertz. In addition, such a system must use a damping mechanism to insure that any vibrations transmitted to the microscope are transient in nature. This damping mechanism is also needed to reduce the vibrations induced by the motion of the sample stage itself in the course of a scan. Finally, an effective isolation system must also shield the NSOM instrument from acoustic vibrations, which fall in the 20Hz to 20kHz range. The isolation system designed under this contract and described in the next section accomplishes all of these objectives.

Although the thermal expansion coefficients of the various components of a NSOM system will vary widely with composition and size, we have found that the components expand/contract roughly 0.1-1.0 micron for every one degree centigrade increase/decrease in temperature. Hence, the differential rate of expansion of the aperture relative to an object has to be surmounted. This obstacle has been overcome by using two lines of attack. First, the entire instrument has been designed to insure that the thermal expansion of the aperture relative to the object is rather small and second, the apparatus is enveloped in a shell that protects against thermal fluctuations.

OVERVIEW OF A PROTOTYPE NSOM

In this section we describe a prototype NSOM instrument built under the present contract in our laboratory. For this description we will use a series of pictures taken during the building of the instrument. Shown in Figure 5 is the vibration isolation system on which the microscope was built. As can be seen it is a passive, dual stage isolation system composed of an optical table and a second stage air table on which the base of the microscope sits. On this base (see Figure 6) rests the sample stage which consists of motorized translators for coarse adjustment and the fine adjustment stage designed by

Wye Creek Instruments. This permits accurate xy positioning with a resolution of $<5\text{nm}$. The sample assembly which permits illumination from the bottom through the rectangular opening seen in the photograph, is surrounded by a stainless steel chamber lined with material for acoustic isolation (see Figure 7). As seen in Figure 8, a conventional optical microscope sits in the side opening of the steel shell and this permits viewing of the pipette as it is translated, with motorized and piezoelectric translators, toward the sample through the opening in the center of the cover. This circular design with the pipette in the center insures that the thermal expansion of the aperture relative to sample is small. Finally, an overview of the microscope is seen in Figure 9. In this overview we clearly see the magnets that we use for eddy current damping of vibrations induced by movements on the stage. These magnets surround the base of the microscope and emanate from pillars that rest on the optical table. The photomultiplier/detection system (not seen in the photograph) that monitors the light emanating from the back end of the pipette is placed on top of the center of the stainless steel shell that surrounds the sample chamber and this signal is recorded, for each position of the sample under the pipette, by one of two IBM PC AT computers. These computers control the scan, collect the data from both the capacitance and NSOM signals and perform the imaging tasks required.

RESULTS FROM THE CORNELL NSOM

In this section we will demonstrate that even in a fluorescence mode the resolution we have obtained with our instrument is comparable to the resolution obtained with scanning electron microscopes. To demonstrate this resolution we made test structures by contact printing a pattern from a mask formed by electron beam lithography. This mask of silicon nitride was placed in contact with a clear glass coverslip and the material to be deposited was then evaporated through the mask and onto the coverslip. For the transmission scans, 50nm of chromium was evaporated whereas 50nm of 3,4,9,10-perylenetetracarboxylic dianhydride was used for the fluorescence measurements. The samples were then coated with 5nm of chromium to assure conductivity over the edge or grating. The patterns thus formed had sharp, well-characterized features as demonstrated by scanning electron microscopy, SEM. Such test patterns are essential to quantitatively assess the resolution of NSOM in both the transmission and fluorescence modes.

Figure 10 shows a transmission scan over a chromium step for both a 600nm and 100nm diameter aperture. The distance from 12% to 88% transmission scales with aperture size. In Figure 11 the high resolution NSOM data is compared to a linescan from an electron micrograph of the same edge. The SEM trace is a convolution of the edge profile with the beam profile and the secondary electron emission yield function. The edge profile can be estimated from the micrograph trace to have a width of 30nm assuming a beam diameter of 20nm. This finite width is a result of the contact printing process. The 12%-88% point in intensity of the NSOM trace is 60nm. This is the near-field beam profile convoluted with the 30nm edge width.

Using these results we can make quantitative comparisons between the SEM and both experimental and theoretical NSOM scans. The theoretical curve through the NSOM data in Figure 11 was generated by assuming exponential absorption in the chromium step and an intensity transmitted to the detector scaling as the third power of the unoccluded area as suggested by Bethe (13).

Also shown in Figure 11 is a conventional far-field optical line scan obtained from the edge using the same 0.55 NA objective lens as used for focusing the light for the NSOM scans. The solid line passing through these experimental points has been calculated from the theory for a conventional incoherent scanning optical microscope (14). The result of a similar calculation for a 1.4NA objective is shown at the top of Figure 11. Thus, one can infer that resolution far exceeding the diffraction limit has been achieved using near-field scanning techniques and this emphasizes the exciting potential of being able to form subwavelength light spots for characterization and fabrication.

Using the same pipettes as were used for the data above we have obtained scans of fluorescent edges and gratings. One such scan of a fluorescent grating of period 800nm is shown in Figure 12A. A densitometer trace of a scanning electron micrograph of the same perylene grating is also shown in Figure 12B. The sharpest maximum and minimum change in the fluorescence NSOM image is <50nm. Thus fluorescence NSOM grating scans have been demonstrated with resolution comparable to the aperture diameter used and comparable to scanning electron micrographs of the same grating. The resolution obtained (15) is at least an order of magnitude better than the emission wavelength which is at 700nm.

WAVELENGTH INDEPENDENT LITHOGRAPHY

Considerable progress has also been made in the development of the necessary experimental methodology to produce the lithographic resists that are necessary for subwavelength lithography. The most successful method uses a Langmuir-Blodgett trough which can produce with high accuracy and reproducibility thicknesses down to a few nanometers. We have shown under this contract that pinhole free layers of such resists can be produced (16). For our initial experiments we used Shipley AZ 1400-5 resist which we were able to spin on as layers of less than 50nm. The scheme we used to impress various patterns on this resist is illustrated in Figure 13A. We developed a combination of a point mount and vacuum suction to bring the substrate into close contact with a quartz mask that was produced by contact printing with aluminum or chrome. Figure 13B shows what is seen when the mask and substrate are viewed from the top. Essentially the black central circle is the region that is within the near-field. The dimensionality of the various components in this scheme is shown in cross-section in Figure 13C. The method of fabrication of the quartz mask is seen in Figure 14. In this figure the pattern which is produced by electron beam lithography is further etched into silicon nitride via reactive ion etching. This mask is used to produce the contact print on quartz. The contact printing process is depicted in Figure 15. As can be seen Cr or Al is thermally evaporated through the silicon nitride mask onto the quartz plate. A scanning electron micrograph of a typical metal on quartz mask is shown in Figure 16. The resulting optical lithograph in the near-field is shown in Figure 17. As can be seen the grating is faithfully reproduced in silicon to better than 200nm resolution using light of 450nm. We expect to get much better resolution once the fabrication quality of our masks is improved with the recently installed electron beam machine at the National Submicron Research and Resource Facility.

In summary, our experiments thus far have demonstrated the feasibility of the subwavelength optical technology we have pioneered under this contract. Thus, these experiments confirm the exciting potential for applications of the near-field technology in a variety of areas of interest to the Air Force.

REFERENCES

1. Ash, E.A. and Nicholls, G., *Nature (Lond.)* 237, 510 (1972).
2. Lewis, A., Isaacson, M., Harootunian, A., and Muray, A., *Ultramicroscopy* 13, 227 (1984).
3. Fisher, U. Ch., *J. Vac. Sci. Technol. B.* 3, 1498 (1985).
4. Durig, U., Pohl, D.W., and Rohner, F., *J. Appl. Phys.* 59, 3318 (1986).
5. Betzig, E., Harootunian, A., Lewis, A., and Isaacson, M., *Appl. Opt.* 25, 1890 (1986).
6. Leviatan, Y., *J. Appl. Phys.* 60, 1577 (1986).
7. Harootunian, A., *Near-Field Scanning Optical Microscopy and Raman Microscopy*, Cornell University Ph.D. Dissertation (1986).
8. Brown, K.T., and Flaming, D.G., *Neuroscience* 2, 813 (1977).
9. Betzig, E., Lewis, A., Harootunian, A., Isaacson, M., and Kratschmer, E., *Biophys. J.* 49, 269 (1986).
10. Matey, J.R., and Blanc, J., *J. Appl. Phys.* 57, 1437 (1985).
11. Binning, G., and Rohner, H., *Helvetica Physica Acta* 55, 726 (1982).
12. Newport Research Corporation Catalog 1983-84, Vol. 13, Fountain Valley, CA.
13. Bethe, H.A., *Phys. Rev.* 66, 163 (1944).
14. Wilson, T., and Shepard, C., *Theory and Practice of Scanning Optical Microscopy*, (Academic Press Inc., London 1984), p. 34.
15. Harootunian, A., Betzig, E., Isaacson, M., and Lewis, A., *Appl. Phys. Lett.* 49, 674 (1986).
16. Schildkraut, J. and Lewis, A., *Thin Solid Films* 134, 13 (1986).

FIGURE CAPTIONS

Figure 1: Schematic representation showing the collimation of radiation emanating from a subwavelength aperture.

Figure 2: The energy flux emanating from a 50nm diameter aperture normalized to the energy of the incident plane wave, is shown plotted as a function of both the perpendicular distance (z) from an 180nm thick conducting screen and the ratio of the lateral distance from the center of the aperture to the half width of the aperture (x/a). Notice that the radiation is collimated to roughly the edge of the aperture ($x/a = 1$) out to $z=60$ nm.

Figure 3: Scanning electron micrographs of metallized pipettes with aperture of diameters 100nm and 500nm at the tips of the pipettes.

Figure 4: Scanning electron micrograph of a 50nm outer diameter pipette.

Figure 5: Shown is the passive vibration isolation system used. Part of the air table used is seen at the bottom of the picture. On this air table is a second stage isolation air table which was home-built and on top of this is placed a Newport surface which serves as the base of the microscope.

Figure 6: Place on the microscope base is the coarse adjustment, motorized translators on which sits a piezoelectric nanometer scanning stage. In the center of this stage sits a circular glass coverslip on which the sample rests. The rectangular opening in the front of the coarse xy stages is for illumination of the sample from the bottom. This is accomplished by a mirror and a long working distance lens that is installed in the stage and focusses the light through the glass coverslip on which the sample sits.

Figure 7: Surrounding the xy stages seen in Fig. 6 is a stainless steel shell that also sits on the microscope base. Lining this shell is material for acoustic shielding.

Figure 8: A stainless steel cover is bolted to the stainless steel shell seen in Fig. 7. In the center of this cover is the opening into which the pipette with the coarse z translator and fine adjustment z piezoelectric fits. In the side of the shell is the microscope which allows the pipette to be viewed as it is brought into proximity of the sample. Also in view at the bottom left hand side of the picture are the optics for the inverted microscope that allows viewing the sample from the bottom as it is translated under the pipette by the coarse stage. Notice that the design decouples the xy motion from the z motion. Thus as the sample is rapidly scanned under the pipette the z piezoelectric, in response to one of the feedback mechanisms described in the text, independently adjusts the z position of the pipette aperture relative to the sample surface so that a constant sample/aperture separation is maintained. Notice also that the circular design minimizes thermal drift problems.

Figure 9: An overview of the NSOM instrument is seen in this figure. Surrounding the instrument are posts that are bolted to the optical table. Each of these posts have magnets that protrude into copper blocks that sit on the base of the microscope. These magnet/copper block assemblies are for eddy

current damping of vibrations that arise from the motions of the microscope during a scan. Seen in the background is the material that forms the walls of the room that surround the microscope. This material provides acoustic isolation. In fact everything except the microscope sits outside this acoustic enclosure. This includes the laser and the two IBM PC AT computers that control the microscope, collect the data and form the images with a special board and a high resolution dedicated graphics system from Imaging Technology. Also seen in the upper right of the picture is the erector set that holds the photomultiplier and detection system. The photomultiplier is placed just above the opening in the stainless steel plate that fits over the stainless steel shell. In this position the photomultiplier can detect the photons that emanate from the back end of the pipette as the sample is translated rapidly under the aperture. Thus, at each position of the sample the photons detected by the photomultiplier are recorded into the memory of one of the two computers and subsequently, within 2secs. after a scan an image appears on the Imaging Technology monitor. This NSOM image can be overlaid with the z topography capacitance image which is available at the same time

Figure 10: Bottom low resolution (aperture=600nm) and top high resolution (aperture=100nm) transmission NSOM scans of a 50nm chromium edge are shown above. Wavelength used was 570nm.

Figure 11: NSOM and SEM comparisons. From bottom to top are shown: a densitometer trace of a scanning electron micrograph of a 50nm thick chromium edge; an NSOM scan of the same edge using 570nm excitation plotted against a theoretical NSOM curve; a theoretical scanning optical microscope (SOM) scan (570nm excitation and NA=0.55) plotted with points from an experimental optical micrograph scan of the same 50nm thick chrome step taken with 570nm excitation and the NA=0.55 optics used for focusing the light on the grating for the NSOM scans; and a theoretical SOM edge scan using a very high (1.4 NA) numerical aperture objective and 570nm excitation. All edge scan steps were normalized to an intensity change of unity.

Figure 12: A fluorescent NSOM and SEM comparison. A fluorescence NSOM scan of a perylene grating with a period of 800nm (A) is shown below a densitometer trace of a SEM scan of the same grating (B). The SEM scan was slightly displaced in a direction parallel to the grating lines relative to the NSOM scan.

Figure 13: A) Schematic of our method of optical pattern transfer B) Top view seen in optical microscope when contact is made between resist and mask C) Cross-sectional view of the optical pattern transfer method.

Figure 14: Method of printing mask fabrication.

Figure 15: Schematic of quartz contact printing.

Figure 16: Scanning electron micrograph of fabricated quartz mask.

Figure 17: A scanning electron micrograph of a near-field replication of a sub-500nm periodicity grating.

PAPERS PUBLISHED UNDER THIS CONTRACT

1. E. Betzig, A. Lewis, A. Harootunian, M. Isaacson and E. Kratschmer, "Near-Field Scanning Optical Microscopy (NSOM)," Biophys. J. 49, 269 (1986).
2. E. Betzig, A. Harootunian, A. Lewis and M. Isaacson, "Near Field Diffraction by a Slit: Implications for Super-Resolution Microscopy," Appl. Optics, 25, 1896 (1986).
3. A. Harootunian, E. Betzig, M. Isaacson, and A. Lewis, "Super-Resolution Fluorescence Near Field Scanning Optical Microscopy," Appl. Phys. Lett. 49, 674 (1986).
4. M. Isaacson, E. Betzig, A. Harootunian and A. Lewis, "Scanning Optical Microscopy at $\lambda/10$ Resolution Using Near Field Imaging Methods" in "Recent Advances in Electron and Light Imaging in Biology and Medicine" Annals of the New York Academy of Sciences, Vol. 483, p. 448 (1986).
5. A. Lewis, E. Betzig, A. Harootunian, M. Isaacson and E. Kratschmer, "Near-Field Imaging of Fluorescence," in Spectroscopic Membrane Probes, ed. Leslie M. Loew (CRC press, 1986).
6. Y. Leviatin, "Study of Near Zone Fields of a Small Aperture," Journal of Appl. Phys. 60, 1577 (1986).
7. E. Betzig, M. Isaacson and A. Lewis, "Collection Mode Near-Field Scanning Optical Microscopy", Appl. Phys. Lett. 51, 2088 (1987).
8. E. Betzig, M. Isaacson, H. Barshatzky, A. Lewis and K. Lin, "Near-Field Scanning Optical Microscopy (NSOM)", Proceedings of SPIE Conference (Los Angeles, 1988).

Ph.D. THESIS

1. A. Harootunian, "Near Field Scanning Optical Microscopy and Raman Microscopy" Ph.D. Thesis, Cornell University, January, 1986.

INVITED LECTURES CONCERNING THE RESEARCH SUPPORTED BY THIS CONTRACT
(SEPT. 1984 - SEPT. 1986).

1. September 1984: Reichart-American Optical Corporation Laboratory, Buffalo, New York. "Near Field Scanning Optical Microscopy", M. Isaacson
2. February 1985: Biophysical Society Meeting, Baltimore, Maryland. "Near Field Scanning Optical Microscopy", A. Lewis
3. March 1986: New York Academy of Sciences, New York City. "Near Field Scanning Optical Imaging", M. Isaacson
4. June 1986: Whitney Symposium on Science and Technology, GE Research and Development Laboratory, Schenectady, New York. "Near Field Optical Imaging", M. Isaacson
5. August 1986: Microbeam Analysis Society Meeting, Albuquerque, New Mexico. "Near Field Scanning Optical Microscopy and Lithography", M. Isaacson
6. September 1986: Tohoku University, Sendai, Japan. "Optical Microscopy at 500Å Resolution", M. Isaacson

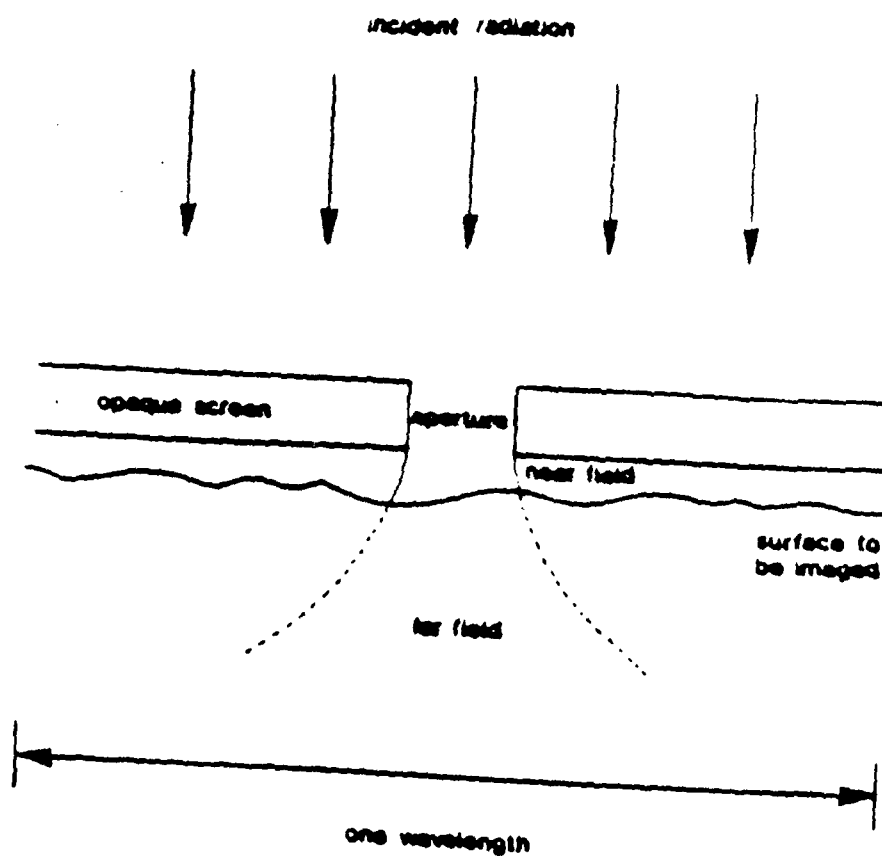


Figure 1

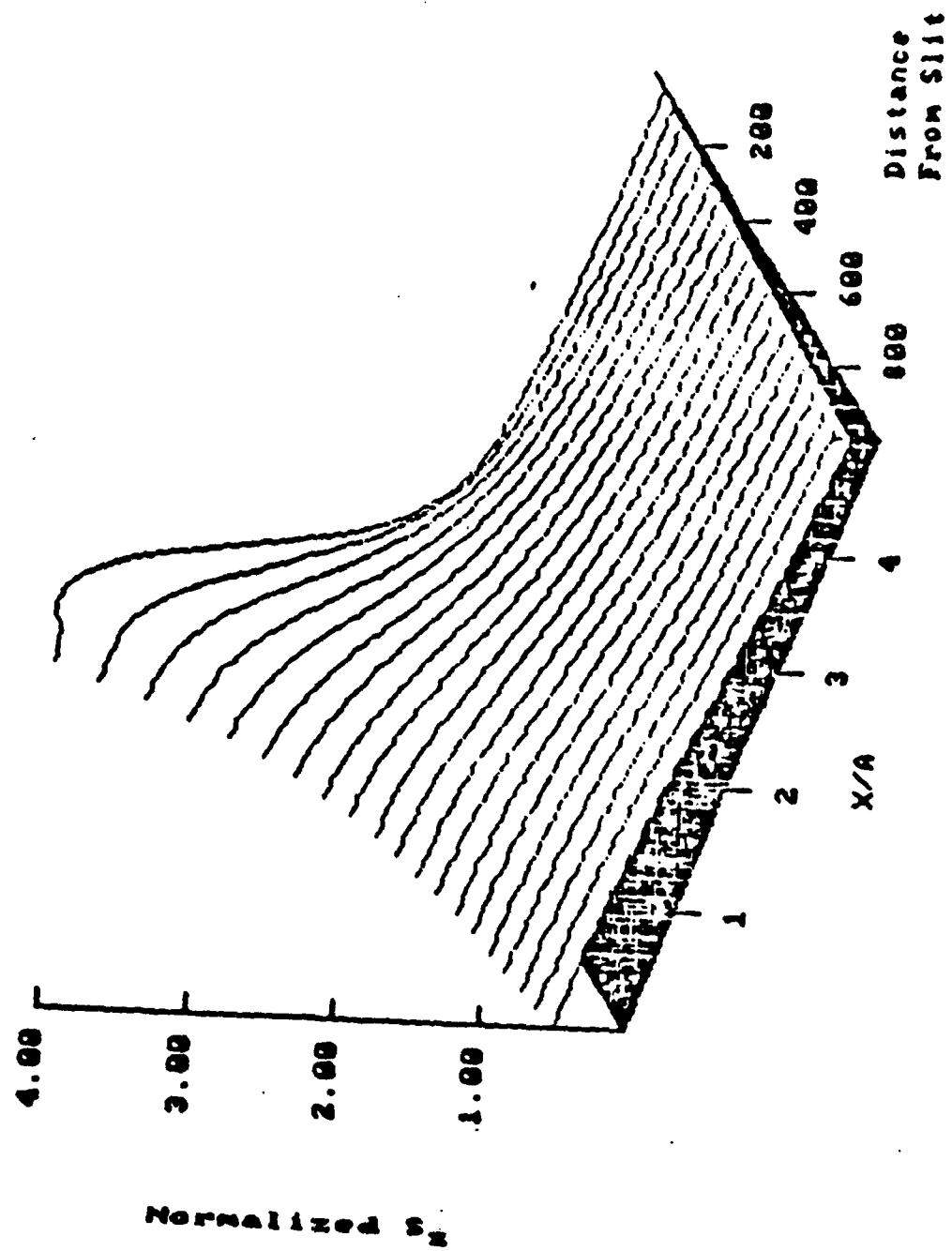


Figure 2

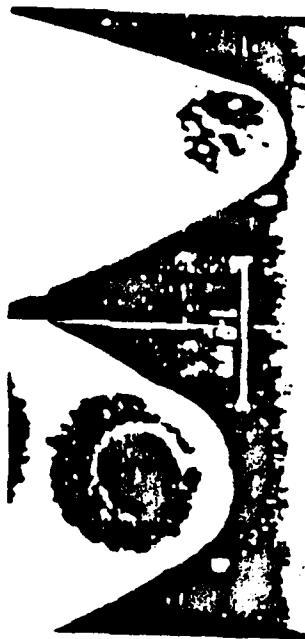


Figure 3

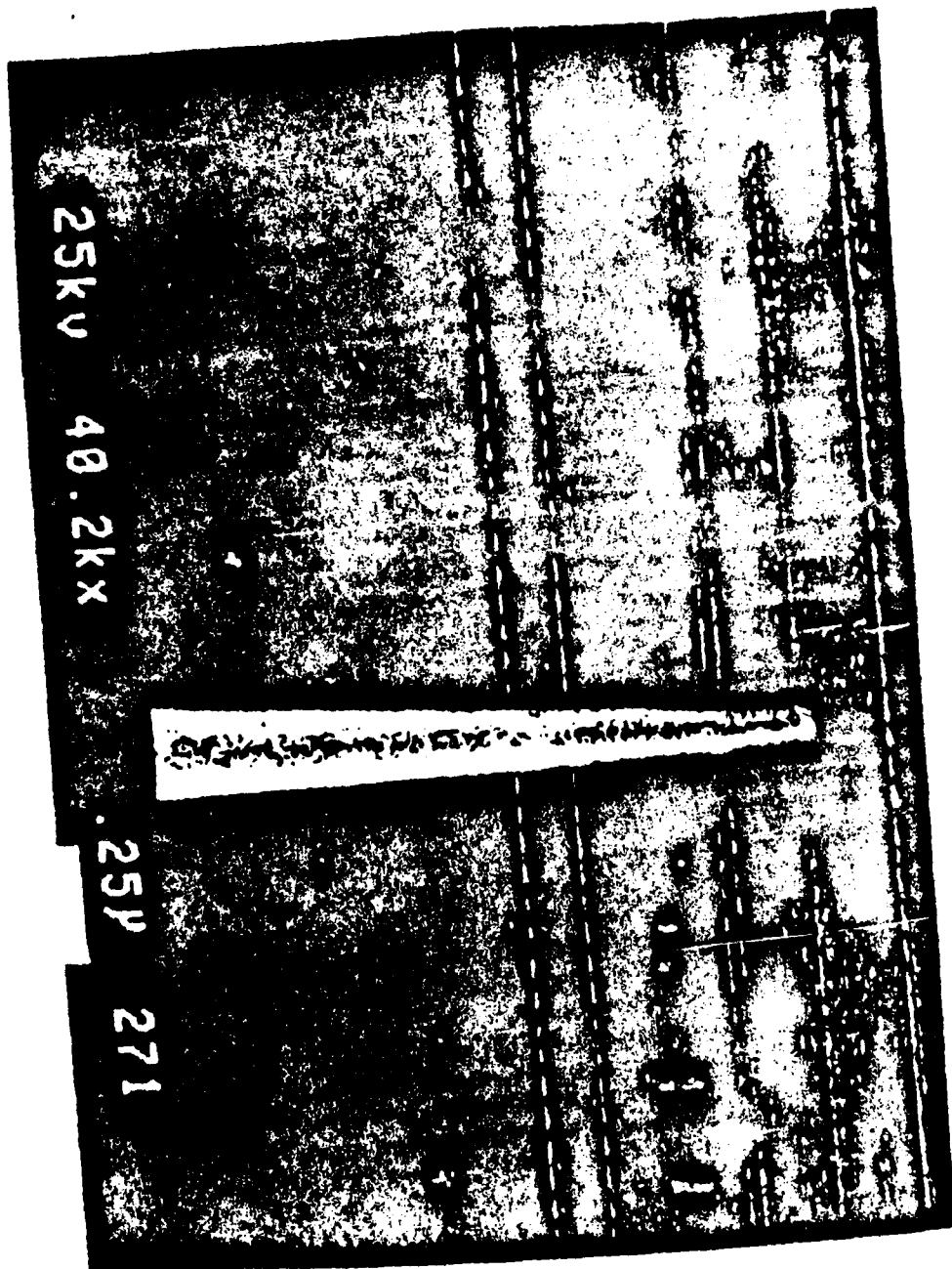
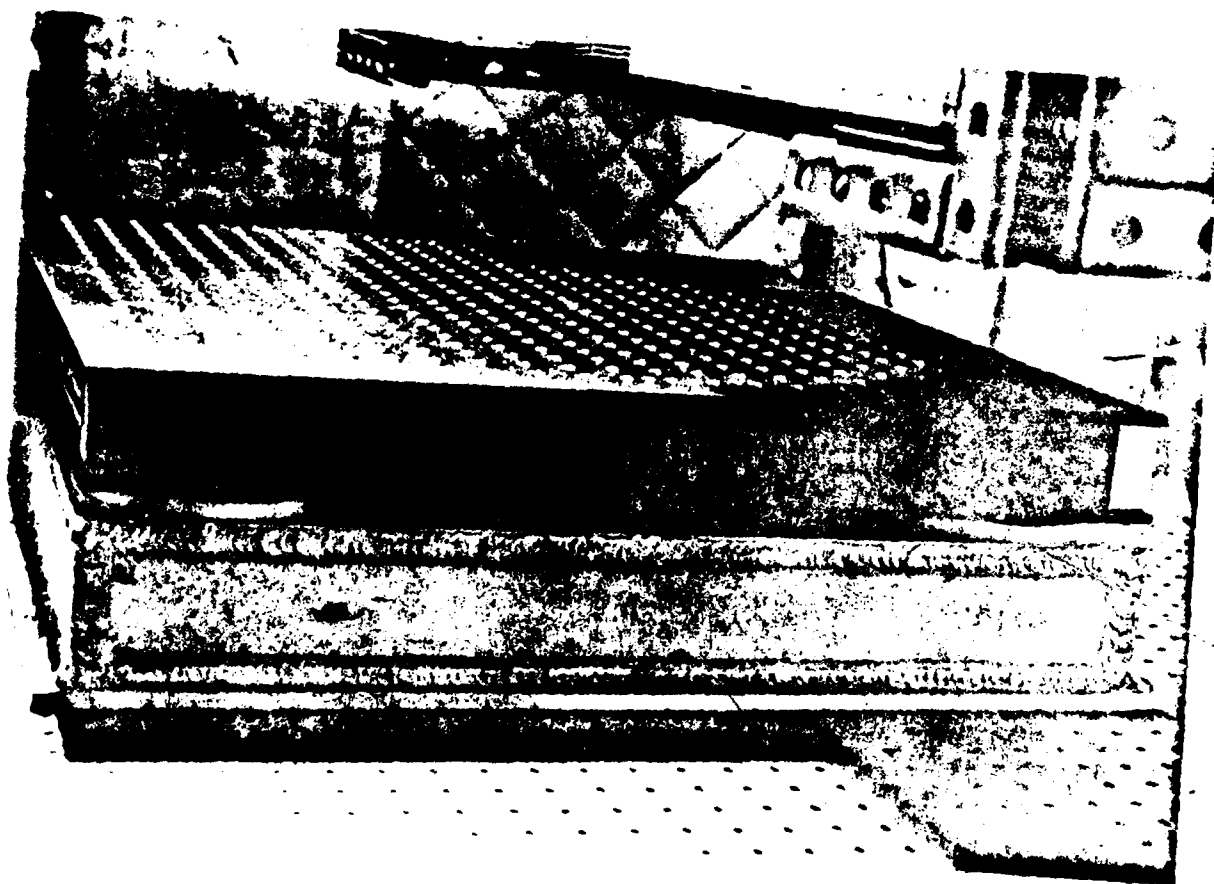
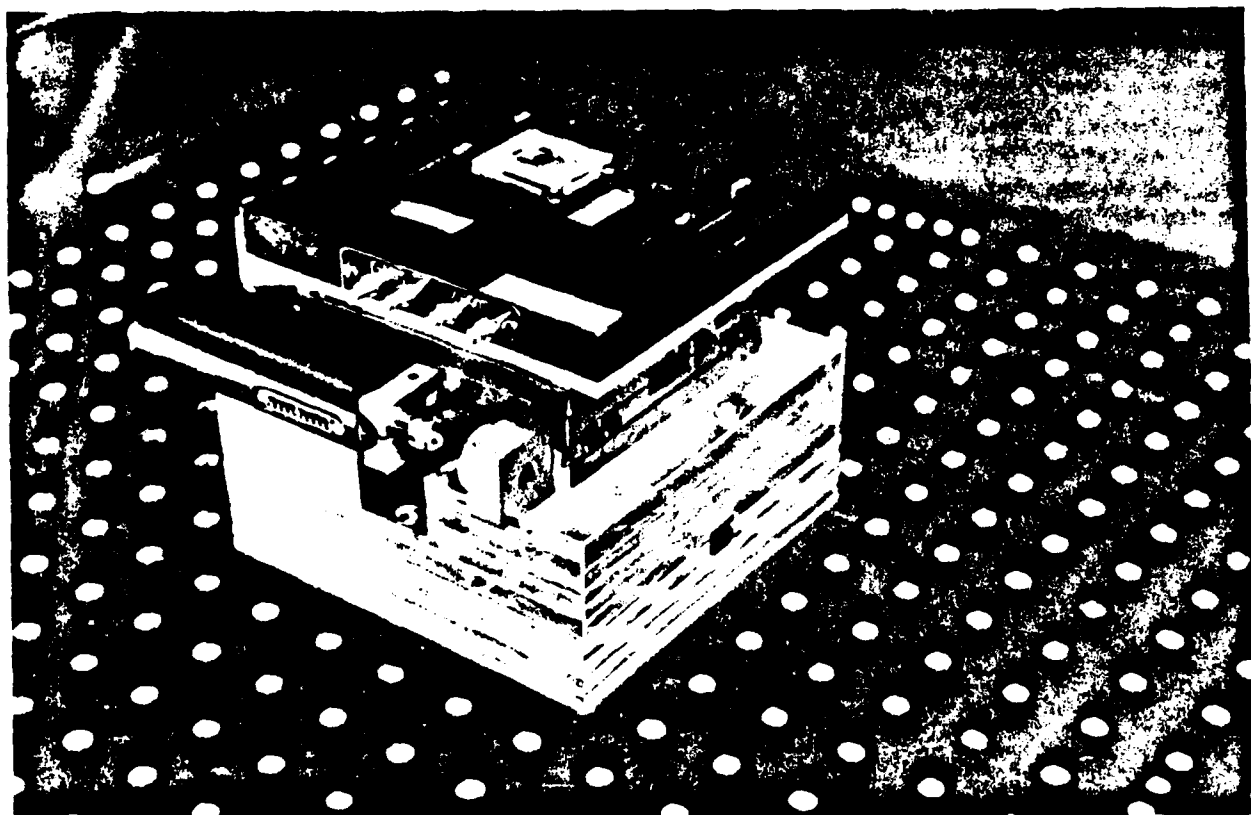
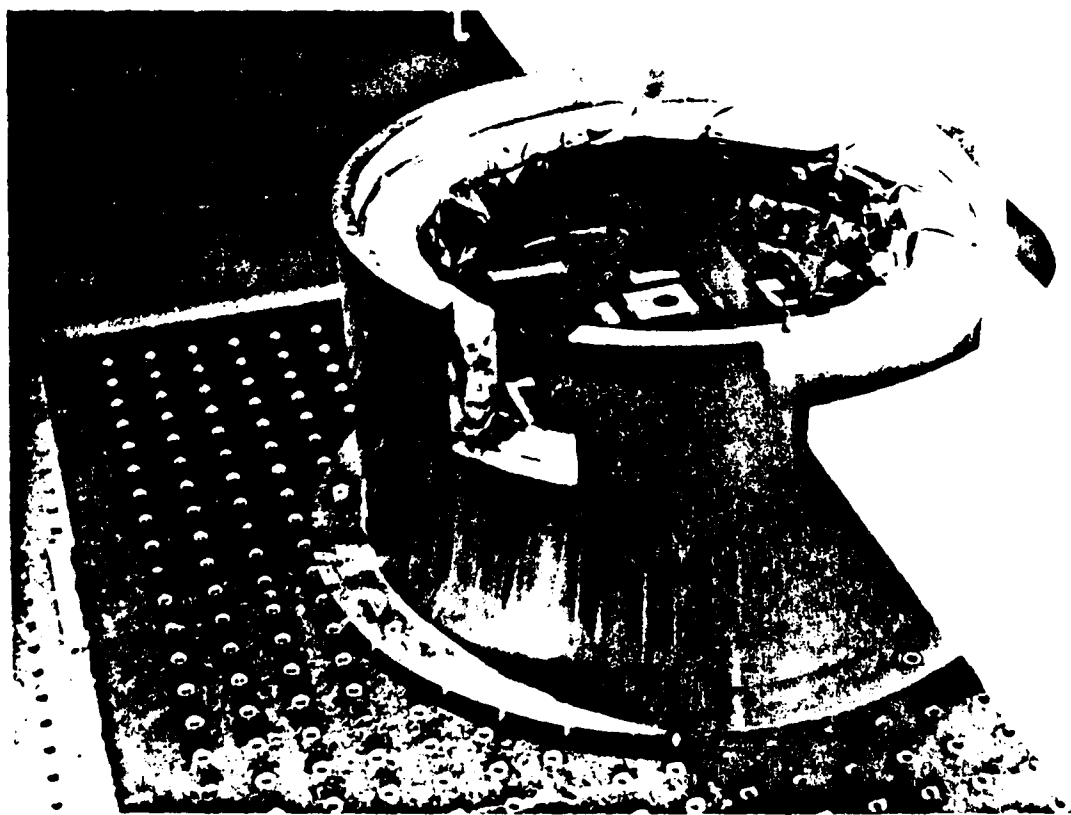


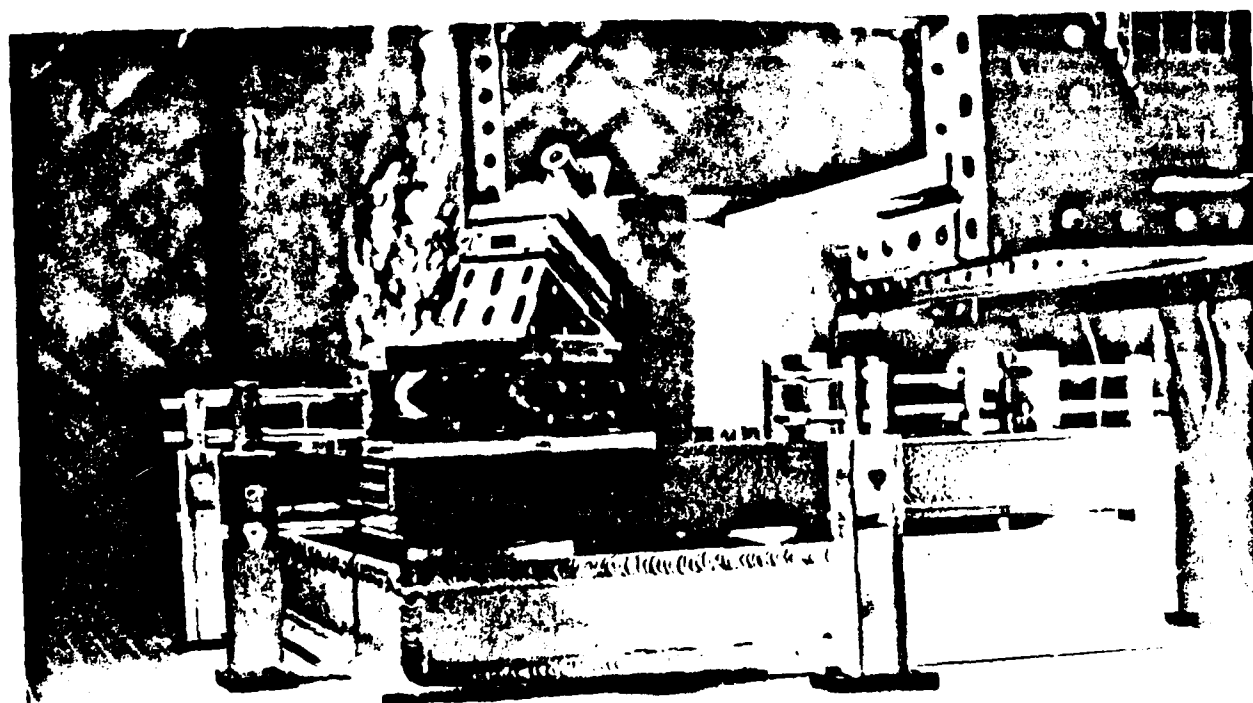
Figure 4











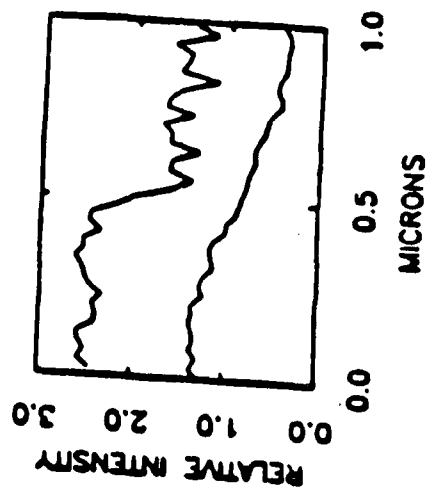


Figure 10

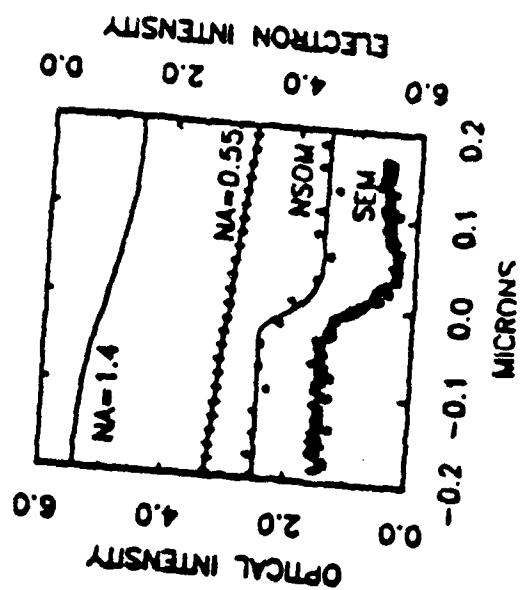


Figure 11

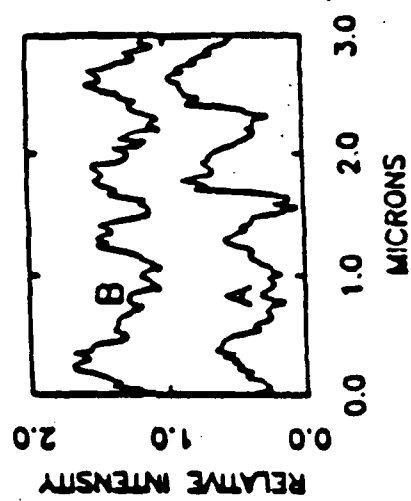


Fig. 12

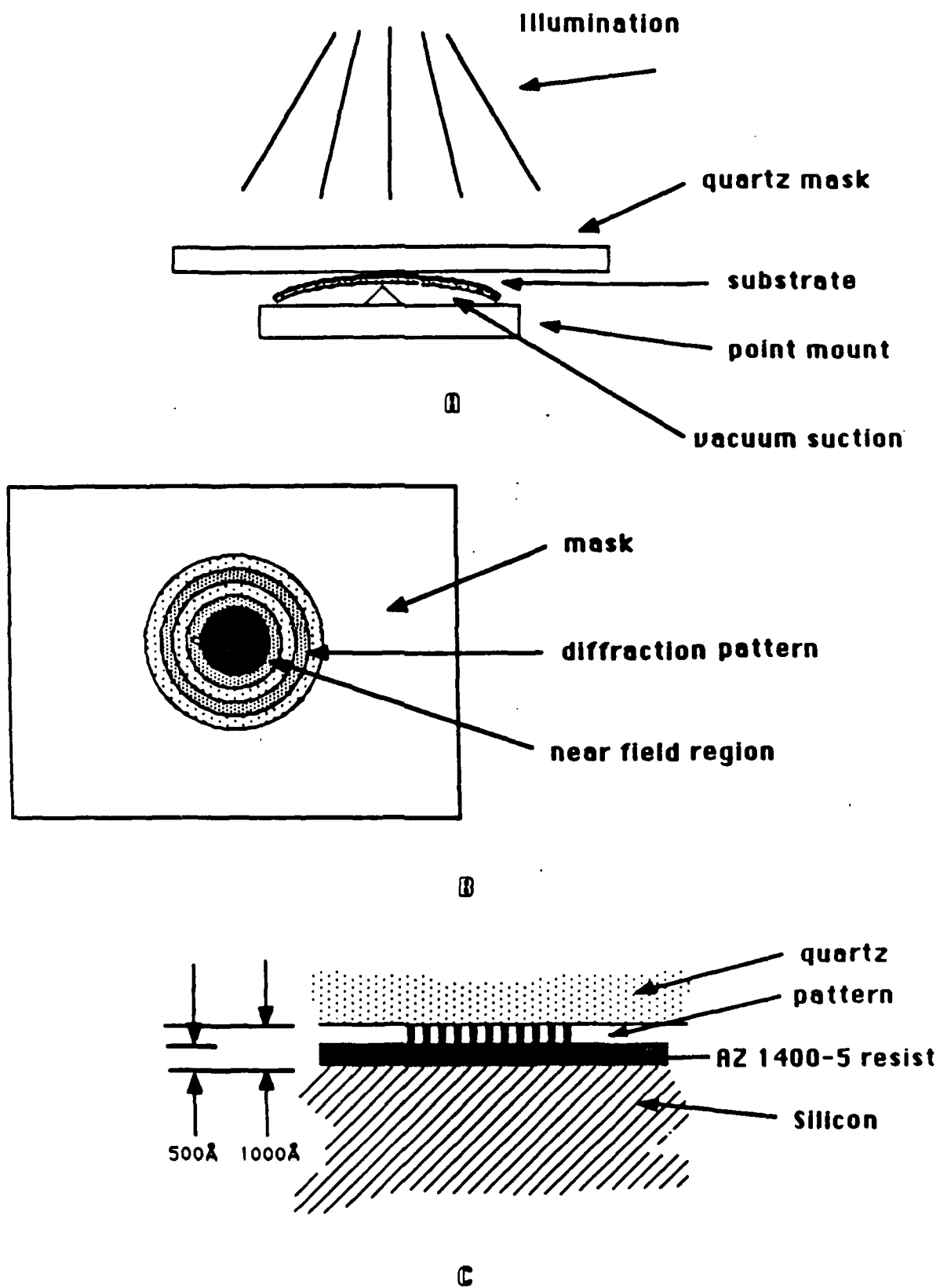


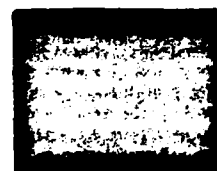
Figure 13

side view

top view



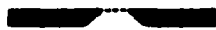
A 1000 μ Si Nitride window is mounted on Si



A layer of PMMA is added

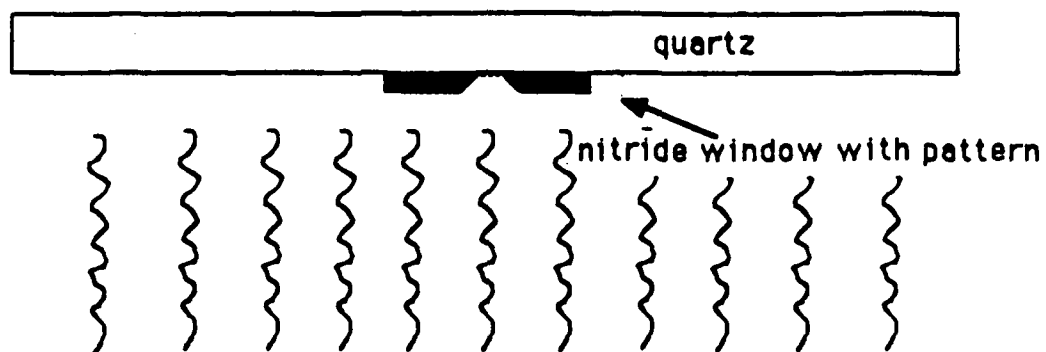


Pattern is exposed with E beam and developed

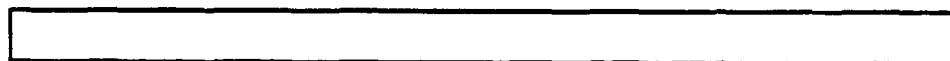


Pattern is etched through Si nitride window

Figure 14

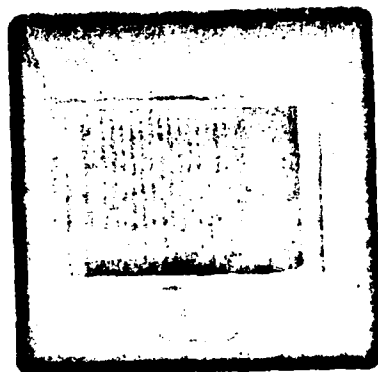


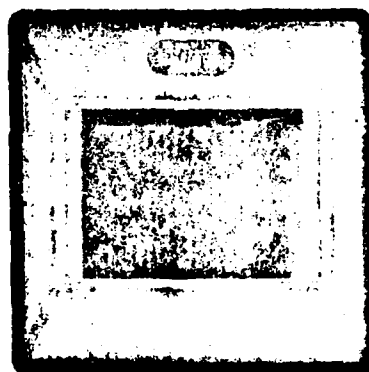
Thermal evaporation of Cr or Al (500 Å)



quartz mask with Cr or Al pattern

Figure 15





Collection mode near-field scanning optical microscopy

E. Betzig, M. Isaacson, and A. Lewis

Cornell University, School of Applied and Engineering Physics, Ithaca, New York 14853

(Received 14 July 1987; accepted for publication 20 October 1987)

Super-resolution imaging at optical wavelengths has been achieved with collection mode near-field scanning optical microscopy. Reproducible images of 0.25- μm aluminum lines separated by 0.25 μm have been generated with a peak edge sharpness of 0.07 μm . Images taken with differing probe sizes and at various heights demonstrate that the smallest resolvable features are roughly determined by the greater of the aperture size and the aperture to sample separation.

In recent years, several groups have demonstrated the feasibility of circumventing the diffraction limit with near-field scanning optical microscopy.¹⁻⁶ In this technique, the light transmitted through a submicron aperture in an opaque screen forms a subwavelength sized spot, which is then scanned over an object to generate a super-resolution image. The resolution is potentially closer to that of a scanning electron microscope than that of a conventional optical microscope, since it is determined by the aperture size. Additional advantages include the use of nondestructive visible radiation, the ability to operate in air, and the use of well-developed optical contrast mechanisms. Hence, the technique could be applied to nondestructive, high-resolution imaging in the semiconductor industry and the biological sciences.

Most of the work in this field has centered around the use of the aperture as an illuminator, with the light transmitted through the sample being collected in the far field by an objective.¹⁻⁴ Fischer² has produced line scans with a reflection instrument, but the technique is only applicable to apertures in a flat screen, so that positioning these apertures within the near field remains a problem. In contrast, we report the first use of collection mode near-field scanning optical microscopy (NSOM), in which the aperture is used as a receiver rather than as a transmitter to collect information from only a small section of an illuminated sample (Fig. 1, right side). This approach is advantageous for three reasons. First, owing to the presence of the incident wave, the geomet-

try for the two modes is not symmetric, and indications suggest that the collection mode may yield higher resolution. Second, luminescent samples (e.g., semiconductor lasers) could be readily imaged with the collection mode. Finally, the collection mode represents the first step towards a form of reflection mode NSOM in which the light from an external illuminator is reflected off the sample and collected by the aperture.

Several steps were involved in constructing the present instrument. Wavelength independent information exists only when the aperture is within the near field relative to the sample. Our numerical calculations⁷ indicate that an aperture to object separation of ≈ 20 nm is needed for ≈ 50 -nm resolution with visible light. The resulting vibration isolation needs were met with a two-stage air table system and sound absorbing curtains. Tunneling measurements yielded a residual vibrational level of ≈ 0.3 nm in a 1-Hz bandwidth from dc. Subnanometer positioning of the aperture relative to the sample was achieved with piezoelectric transducers (Fig. 1). The aperture was moved vertically to within the near field using a piezoelectric tube, and the lateral scan pattern was produced by moving the sample with a commercial, low hysteresis stage.⁸ A 75-W xenon arc lamp with an UV cutoff filter (400 nm) provided uniform illumination over the entire visible range to minimize standing wave effects between the sample and the aperture screen.⁷ The light was focused with a 15×0.28 numerical aperture objective onto

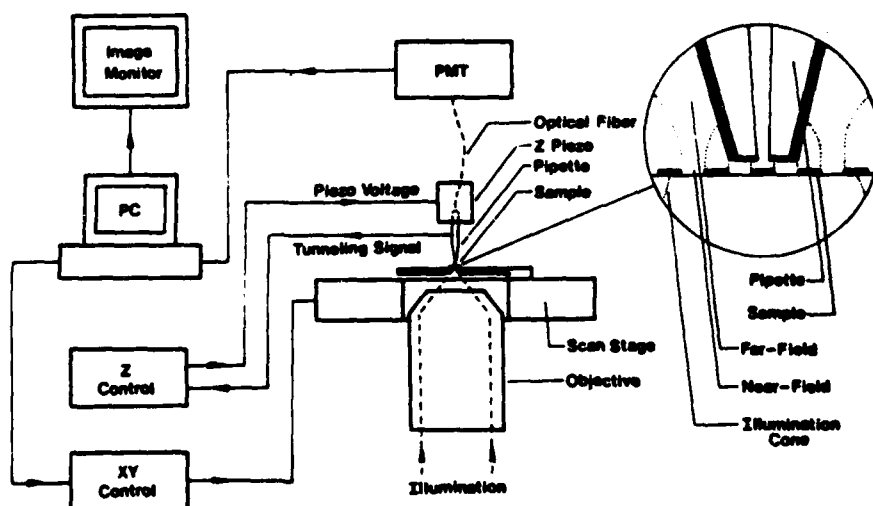


FIG. 1. At left is shown a schematic of the instrument used for collection mode near-field scanning optical microscopy (NSOM). At right, an expanded view is shown of the light transmitted through a sample being collected in the near field by an aperture. Within the near field, spatial resolution is determined by the aperture size, which could be as small as 50 nm. In the far field the resolution is wavelength limited.

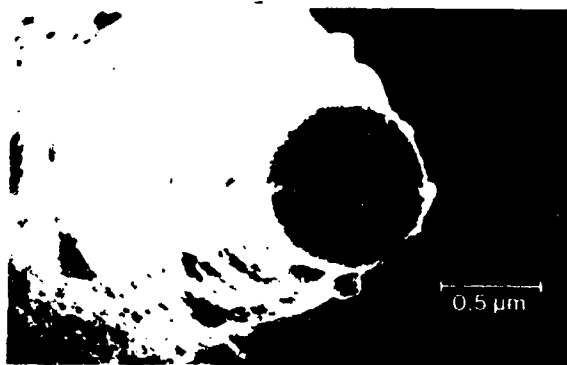


FIG. 2. Aluminum coated pipette with an outer diameter of 800 nm and an aperture diameter of 150 nm, typical of those used for the images in this work.

the sample. Transmitted light collected by the aperture within the near field was sent to a photomultiplier via an optical fiber. A computer was used to synchronize the xy scan pattern to the collection of intensity data, which appeared on the monitor to form a complete digital image.

Two aspects of the design merit special attention. To scan recessed regions of rough surfaces and remain within the near field, it is necessary to produce an aperture within a sharply tapered probe. We have accomplished this by pulling heated glass capillaries past the breaking point. The resulting pipettes are evaporated with 50 nm of aluminum on the tip and 200 nm on the sides to create a structure which is completely opaque except for the central aperture. This technique is rapid, inexpensive, and highly reproducible. We have produced outer diameters of 30 nm–30 μ m and aperture diameters of 50 nm–10 μ m by this method. Figure 2 shows an aluminum coated pipette with an 800-nm diameter and a 150-nm aperture.

To sense the surface and remain within the near field, a distance regulation mechanism is also needed. At present, we have tried three methods. Tunneling feedback⁹ has been used to maintain an aperture-sample separation of < 1 nm. Both the sample and the aluminized pipettes are coated with 20 nm of gold to ensure conductivity in this mode. The resulting images are rather poor and contain numerous streaks. We speculate that the pipette may be occasionally forced to push through an insulating layer of absorbed contaminants to maintain a constant tunneling current, thus causing the tip to drag. This problem, when coupled with its

slow speed, may restrict the applicability of tunneling in near-field microscopy.

Another method to reach the near field involves producing images at successively closer distances until the desired resolution is obtained. This constant height mode is only applicable to very flat samples or flat regions on a rough sample. However, since the speed is limited only by the intensity of the optical signal, good quality images are formed quite rapidly.

Finally, in contact mode the pipette is advanced towards the surface until a tunneling current is measured, but no feedback is used in the ensuing scan. Over flat samples the pipette is apparently sufficiently flexible and the contact force sufficiently low so that neither the tip nor the sample is damaged, and minimal streaking occurs.

Electron beam lithography was used to fabricate gratings to test the resolution of the microscope.¹⁰ A representative grating is shown in Fig. 3(a), consisting of 250-nm-wide, 100-nm-high aluminum lines separated by 250 nm on a transparent, 100-nm-thick membrane of silicon nitride. The edge sharpness of these lines is on the order of 200 Å. The corresponding NSOM micrograph of a similar grating is shown in Fig. 3(b), where the opaque aluminum lines appear as black stripes. All of the lines are clearly reproduced. The contact mode was used, as is evident from the slight streak in the upper right corner of Fig. 3(b). A pipette similar to that shown in Fig. 2 collected the light, and an average signal of ≈ 2 pW was obtained. The complete 512×512 pixel image covering $7.5 \times 7.5 \mu$ m was formed in 10 min.

Reproducibility of the instrument, even in the contact mode, is demonstrated in Fig. 4. The two images of the same grating have many common features, such as slight modulations in the widths of the lines. Once a pipette has been positioned appropriately over the sample, the production of good images is quite routine. We have found no limit on the number of scans which can be performed with a single pipette. One interesting feature of all the near-field images is the existence of strong intensity maxima present at the corners of the aluminum lines. These may result from high local electric fields presumably due to the high conductivity and sharp corners of the aluminum lines.

Within the near field, the true resolution is determined by the aperture size, since two features separated by less than the aperture size will produce a convoluted intensity profile. On the other hand, the sharpness of an isolated edge can be significantly less than the aperture diameter. Using the



FIG. 3. (a) Scanning electron micrograph of an aluminum test pattern on a transparent silicon nitride film. (b) Near-field optical micrograph of a similar grating.

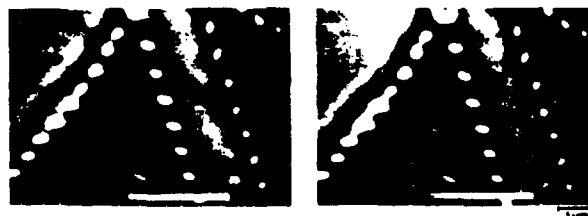


FIG. 4. Two successive scans of the same grating demonstrate the reproducibility of the instrument operating in the contact mode.



FIG. 5. Two images of the same grating taken at a height of ≈ 600 nm with aperture sizes of (a) ≈ 600 nm and (b) ≈ 150 nm demonstrate the effect of aperture size on resolution.

12%–88% transmission points as a criterion and assuming the collected intensity is proportional to the third power of the unoccluded aperture area,¹¹ an edge sharpness of 0.42 diameters is expected. Sections taken through the NSOM images yield an average edge sharpness of 120 nm, although features as small as 70 nm can be found. From Figs. 3 and 4, the true resolution is clearly better than 250 nm. Further claims concerning the true resolution await the production of finer gratings.

To test the effect of the aperture size on the resolution, two images of the same grating were taken with apertures of different sizes. For Fig. 5(a), an ≈ 600 -nm aperture was produced by using a pipette similar to that shown in Fig. 2, except that the aluminum evaporation of the flat tip was omitted, so that the entire tip served as an aperture. For Fig. 5(b), the tip evaporation was included to produce an ≈ 150 -nm aperture. In both cases, the scans were taken in the constant height mode at a distance of ≈ 600 nm. A comparison of the images indicates that the resolution is indeed dependent upon aperture size.

Finally, to demonstrate the effect of the aperture to sample separation on the resolution, a series of images was obtained as the pipette approached the surface. In Figs. 6(a) and 6(b), where the separations were 780 and 330 nm, respectively, the resolution is limited by the separation. In Fig. 6(c), the height of the pipette was equal to the presumed aperture size of 150 nm, and hence the image represents the situation at the outer fringe of the near field. The resolution and edge sharpness in this case is only slightly poorer than in the contact scan in Fig. 6(d), where the resolution is determined solely by the aperture size.

Currently we are working to extend these results by pro-

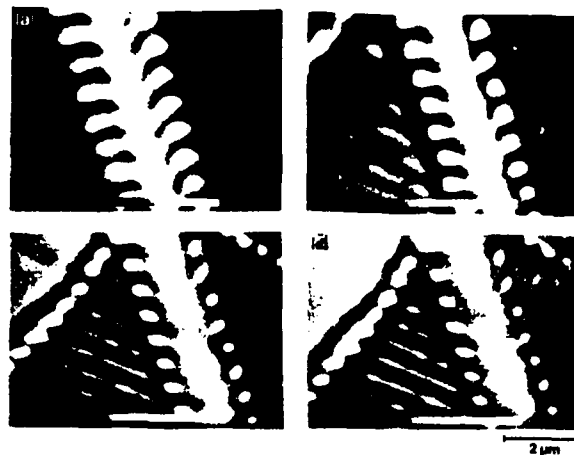


FIG. 6. Images generated at aperture to sample separations of approximately (a) 780 nm, (b) 330 nm, (c) 150 nm, and (d) in contact demonstrate the effect of the separation on the resolution. Differences between (c) and (d) are small, since the separation is comparable to the aperture size in (c).

ducing smaller apertures and finer gratings. To permit near-field scanning over rough surfaces, a feedback mechanism based on capacitance microscopy¹² is also being developed.

We wish to thank Ken Lin, Harry Barshatsky, Jim Strickler, Andy Thompson, and John Koumjian for their valuable contributions. This work is supported by the National Science Foundation contract ECS-8410304 and U.S. Air Force contract AFOSR-84-0314. Gratings were fabricated at the National Nanofabrication Facility (National Science Foundation grant ECS-8619049). E. B. is supported as an IBM Graduate Fellow.

¹E. Betzig, A. Lewis, A. Harootunian, M. Isaacson, and E. Kratschmer, *Biophys. J.* **49**, 269 (1986).

²A. Harootunian, E. Betzig, M. Isaacson, and A. Lewis, *Appl. Phys. Lett.* **49**, 674 (1986).

³D. W. Pohl, W. Denk, and M. Lanz, *Appl. Phys. Lett.* **44**, 652 (1984).

⁴U. Dürig, D. W. Pohl, and F. Rohner, *J. Appl. Phys.* **59**, 3318 (1986).

⁵U. Ch. Fischer, *J. Vac. Sci. Technol. B* **3**, 386 (1985).

⁶U. Ch. Fischer, *J. Opt. Soc. Am. B* **3**, 1239 (1986).

⁷E. Betzig, A. Harootunian, A. Lewis, and M. Isaacson, *Appl. Opt.* **25**, 1890 (1986).

⁸F. E. Scire and E. C. Teague, *Rev. Sci. Instrum.* **49**, 1735 (1978).

⁹G. Binnig, H. Rohrer, Ch. Gerber, and E. Weibel, *Phys. Rev. Lett.* **50**, 120 (1983).

¹⁰E. Kratschmer and M. Isaacson, *J. Vac. Sci. Technol. B* **4**, 361 (1986).

¹¹H. A. Bethe, *Phys. Rev.* **66**, 163 (1944).

¹²J. R. Matey and J. Blanc, *J. Appl. Phys.* **57**, 1437 (1985).

Near-field diffraction by a slit: implications for superresolution microscopy

Eric Betzig, A. Harootunian, A. Lewis, and M. Isaacson

The transmission of light through an infinite slit in a thick perfectly conducting screen is investigated. The spatial distribution of the near-field energy flux is determined through the formulation of four coupled integral equations, which are solved numerically. Transmission coefficients calculated by this method are in agreement with those determined by an alternative formulation. The results theoretically demonstrate the feasibility of near-field superresolution microscopy, in which the collimated radiation passed by an aperture is used to circumvent the diffraction limit of conventional optics, and further suggest the feasibility of near-field superresolution acoustic imaging.

1. Introduction

The transmission of radiation through small apertures has been investigated for a number of years. Bethe¹ treated the case of diffraction by a round hole in an infinitely thin perfectly conducting screen in the limit where the hole was small compared to the wavelength and considered the applicability of his solution to frequency behavior and power flow in microwave cavities. More recently, research in aperture diffraction has been aimed at obtaining a better understanding of the effects of nuclear-induced electromagnetic pulses.² However, these studies have not dealt with the near-field spatial distribution of radiation transmitted past the aperture. The development by Ash and Nicholls³ of a scanning microwave microscope with $\lambda/60$ resolution provides the incentive to apply aperture diffraction theory to a new problem: the determination of the practical limits of near-field superresolution microscopy. Although in this paper we will consider the specific case of optical microscopy, the results are applicable to other regimes of the electromagnetic spectrum.

In the near-field microscope, an illuminated subwavelength aperture is used as a light source. This aperture is then placed within the near field relative to an object, and an image is generated by scanning the aperture relative to the object (see Fig. 1). From a

theoretical standpoint, the most interesting questions concern the degree of collimation of the radiation immediately past the screen and the rate of spreading of the radiation farther from the screen, which would determine the resolution capabilities and positioning requirements of a superresolution instrument. To address these questions, a 2-D aperture model will be considered, i.e., an infinite slit in a thick screen of perfect conductivity.

The infinite slit geometry has already been considered by a number of researchers. Harrington and Auckland⁴ have analyzed the problem using the method of moments and developed a simple equivalent circuit in the narrow slit limit (width $\ll \lambda$). However, their results are concerned primarily with transmission coefficients rather than the spatial distribution of the radiation. Neerhoff and Mur⁵ have used a Green's function formulation for the problem. Indeed their derivation will be used for the analysis here and is summarized below. The difference between this work and that of Neerhoff and Mur lies in the manner in which the model is applied. First, the smallest slits considered by Neerhoff and Mur were $\sim \lambda/2$ in width, whereas much smaller slits (width $\approx \lambda/10$) are of interest in superresolution applications. Second, although the authors compare the electromagnetic field amplitudes in the plane of the slit with similar amplitudes farther from the screen, the down-screen distances chosen for comparison are generally beyond the range of collimation as determined by the more thorough calculations included in this work. Finally, when considering illumination for microscopic or photolithographic applications, the energy flux transmitted by the slit is of greater physical significance than are the field amplitudes calculated by Neerhoff and Mur.

In short, the theoretical development of Neerhoff and Mur will be used to find the fields at the bound-

The authors are with Cornell University, School of Applied & Engineering Physics, Ithaca, New York 14853.

Received 23 December 1985.

0003-6935/86/121890-11\$02.00/0.

© 1986 Optical Society of America.

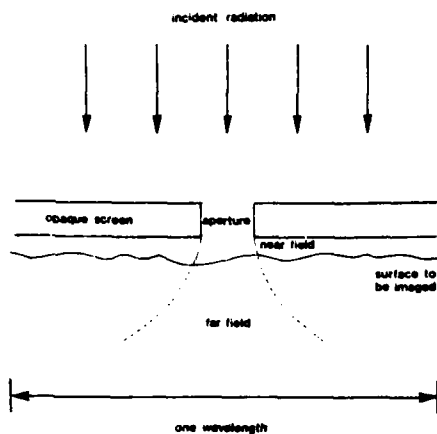


Fig. 1. Geometry of the near-field scanning optical microscope.

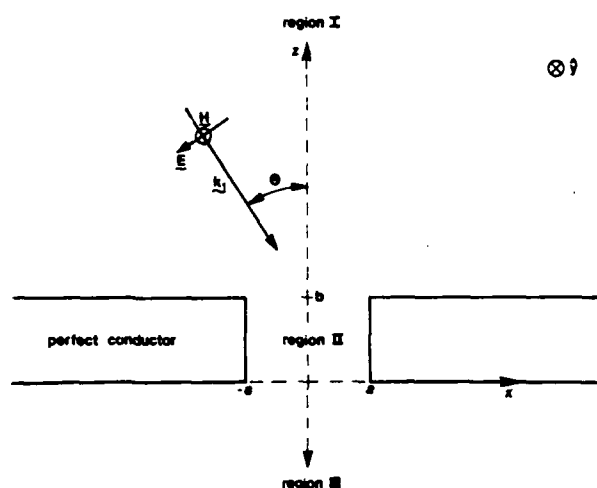


Fig. 2. Model for diffraction by a slit in a thick screen.

aries of a number of narrow slits, and these fields will then be used to calculate the spatial distribution of the transmitted energy flux within the near field. To check the consistency of the results, transmission coefficients will be calculated and compared to the findings of Harrington and Auckland. The implications of the results for superresolution microscopy will then be discussed.

II. Theoretical Development

A. Initial Formulation

The following formulation summarizes the work of Neerhoff and Mur. The notation used has also been largely adopted from that work.

The configuration appropriate for the formulation of the problem is shown in Fig. 2. The slit, with width $2a$, is chosen parallel to the y axis and is contained in a screen of thickness b . The space surrounding the slit is divided into three regions. Region I ($|x| < \infty, |y| < \infty, b < z < \infty$) contains the space above the slit and

includes the incident electromagnetic wave. Region II ($|x| < a, |y| < \infty, 0 < z < b$) contains the space inside the slit. Finally, region III ($|x| < \infty, |y| < \infty, -\infty < z < 0$) contains the space below the slit and includes the transmitted wave. Different dielectrics can exist in the different regions.

The incident plane wave in region I propagates in the x - z plane at an angle θ with respect to the z axis. The magnetic field is assumed to be time harmonic and both polarized and constant in the y direction:

$$H(x, y, z, t) = U(x, z) \exp(-i\omega t) \hat{e}_y. \quad (1)$$

These restrictions are placed for two reasons. First, elementary waveguide calculations indicate that at least one propagating mode exists for this polarization, no matter how narrow the slit. Hence the arrangement is of physical interest, since large transmission coefficients can be anticipated. Second, Maxwell's equations can be used to find the electric field from $U(x, z)$:

$$E_x(x, z) = -\frac{ic}{\omega\epsilon} \partial_z U(x, z); \quad (2a)$$

$$E_y(x, z) = 0; \quad (2b)$$

$$E_z(x, z) = \frac{ic}{\omega\epsilon} \partial_x U(x, z). \quad (2c)$$

Thus the restrictions in Eq. (1) reduce the diffraction problem to one involving a single scalar field in only two dimensions.

The field is represented by $U_j(x, z)$ ($j = 1, 2, 3$) in each of the three regions. The time harmonic behavior indicates that the field satisfies the Helmholtz equation:

$$(\nabla^2 + k^2)U_j = 0 \quad (j = 1, 2, 3). \quad (3)$$

In region I the field is further decomposed into three components:

$$U_1(x, z) = U^i(x, z) + U^r(x, z) + U^d(x, z), \quad (4)$$

each of which satisfies

$$(\nabla^2 + k^2)U^{i,r,d} = 0. \quad (5)$$

U^i represents the incident field, which, for simplicity, is assumed to be a plane wave of unit amplitude:

$$U^i(x, z) = \exp[ik_1(x \sin\theta - z \cos\theta)] \quad |\theta| < \pi/2. \quad (6)$$

U^r denotes the field that would be reflected if there were no slit in the screen and thus satisfies

$$U^r(x, z) = U^i(x, 2b - z). \quad (7)$$

U^d describes the diffracted field in region I due to the presence of the slit.

For a perfectly conducting screen, the tangential E vanishes at the surface so that

$$\partial_n U = 0 \text{ at the conductor surface,} \quad (8)$$

where n is the normal vector at the surface. Further boundary conditions result from assuming that the diffracted fields vanish at infinity:

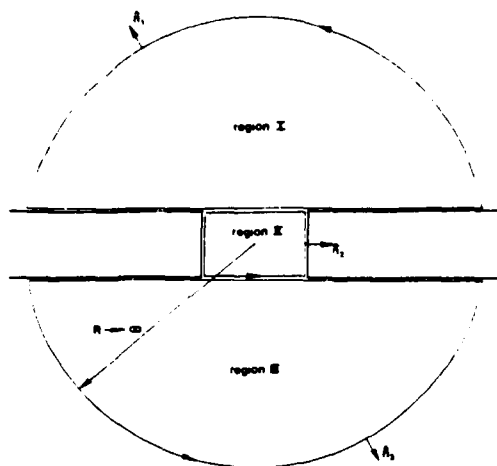


Fig. 3. Regions of integration used for the boundary value problem.

$$U_d, U_3 \rightarrow o(1/R) \text{ as } R \rightarrow \infty; \quad (9a)$$

$$\partial_n U_d, \partial_n U_3 \rightarrow o(1/R) \text{ as } R \rightarrow \infty. \quad (9b)$$

The final boundary conditions are valid at the upper and lower slit boundaries:

$$U_1(x, z)|_{z \rightarrow b^+} = U_2(x, z)|_{z \rightarrow b^-} \quad \text{for } |x| < a; \quad (10a)$$

continuity of tangential H

$$U_2(x, z)|_{z \rightarrow 0^+} = U_3(x, z)|_{z \rightarrow 0^-} \quad \text{for } |x| < a; \quad (10b)$$

$$\epsilon_2 \partial_z U_1(x, z)|_{z \rightarrow b^+} = \epsilon_1 \partial_z U_2(x, z)|_{z \rightarrow b^-} \quad \text{for } |x| < a; \quad (11a)$$

continuity of tangential E

$$\epsilon_3 \partial_z U_2(x, z)|_{z \rightarrow 0^+} = \epsilon_2 \partial_z U_3(x, z)|_{z \rightarrow 0^-} \quad \text{for } |x| < a. \quad (11b)$$

With the above set of equations and boundary conditions, a unique solution exists for the diffraction problem.

B. Development of Integral Field Representations

To find the field, the 2-D Green's theorem is applied with one function given by $U(x, z)$ and the other by a standard Green's function:

$$(\nabla^2 + k^2)G_j = -\delta(x - x', z - z') \quad (j = 1, 2, 3), \quad (12)$$

where (x, z) refers to a field point of interest, and x', z' are integration variables. Since U_j satisfies Eq. (3), Green's theorem reduces to

$$U(x, z) = \int_{\text{Boundary}} (G \partial_n U - U \partial_n G) dS, \quad (13)$$

where the boundaries are shown in Fig. 3.

By virtue of Eq. (8), more is known about $\partial_n U$ at the boundaries than is known about U itself. Hence we impose boundary conditions on G :

$$\partial_z G_1(x, z)|_{z \rightarrow b^+} = 0 \quad \text{for } |x| < \infty; \quad (14a)$$

$$\partial_z G_3(x, z)|_{z \rightarrow 0^-} = 0 \quad \text{for } |x| < \infty; \quad (14b)$$

$$\partial_z G_2(x, z)|_{z \rightarrow a^-} = 0 \quad \text{for } 0 < z < b; \quad (14c)$$

$$\partial_z G_2(x, z)|_{z \rightarrow -a^+} = 0 \quad \text{for } 0 < z < b. \quad (14d)$$

Furthermore, G_1 and G_3 must satisfy the Sommerfeld radiation condition:

$$G_1, G_3(r, t) \propto \exp[-i(\omega t - \vec{k} \cdot \vec{r})] \text{ as } |r| \rightarrow \infty. \quad (15)$$

The equations of this section permit complete evaluation of the three Green's functions. In regions I and III we find

$$G_1(x, z; x', z') = \frac{i}{4} [H_0^{(1)}(k_1 R) + H_0^{(1)}(k_1 R')], \quad (16a)$$

$$G_3(x, z; x', z') = \frac{i}{4} [H_0^{(1)}(k_3 R) + H_0^{(1)}(k_3 R'')], \quad (16b)$$

where

$$R = \sqrt{(x - x')^2 + (z - z')^2}, \quad (17a)$$

$$R' = \sqrt{(x - x')^2 + (z + z' - 2b)^2}, \quad (17b)$$

$$R'' = \sqrt{(x - x')^2 + (z + z')^2}. \quad (17c)$$

In region II, the method of images can be used. The result is given by Morse and Feshbach⁶:

$$G_2(x, z; x', z') = \frac{i}{4a\gamma_0} \exp(i\gamma_0|z - z'|) + \frac{i}{2a} \sum_{m=1}^{\infty} \gamma_m^{-1} \times \cos\left[\frac{m\pi(x+a)}{2a}\right] \cos\left[\frac{m\pi(x'+a)}{2a}\right] \times \exp(i\gamma_m|z - z'|), \quad (18)$$

where

$$\gamma_m = \sqrt{k^2 - \left(\frac{m\pi}{2a}\right)^2} \quad \text{Re}(\gamma_m) \geq 0 \quad \text{Im}(\gamma_m) \geq 0. \quad (19)$$

With these explicit representations for G and the boundary conditions on both G and U , the integral representation for U given in Eq. (13) can be simplified. Furthermore, with the continuity conditions at the slit boundaries, U can be written exclusively in terms of U_2 and $\partial_z U_2$ at these boundaries. We find

$$U^d(x, z) = - \int_{-a}^a \left(\frac{\epsilon_1}{\epsilon_2} \right) G_1(x, z; x', b) DU_b(x') dx' \quad \text{for } b < z < \infty, \quad (20a)$$

$$U_3(x, z) = \int_{-a}^a \left(\frac{\epsilon_3}{\epsilon_2} \right) G_3(x, z; x', 0) DU_0(x') dx' \quad \text{for } -\infty < z < 0, \quad (20b)$$

$$U_2(x, z) = - \int_{-a}^a [G_2(x, z; x', 0) DU_0(x') - U_0(x') \partial_z G_2(x, z; x', z')|_{z \rightarrow 0^+}] dx + \int_{-a}^a [G_2(x, z; x', b) DU_b(x') - U_b(x') \partial_z G_2(x, z; x', z')|_{z \rightarrow b^-}] dx \quad \text{for } |x| < a \text{ and } 0 < z < b, \quad (20c)$$

where the boundary fields are defined by

$$U_0(x) \equiv U_2(x, z)|_{z \rightarrow 0^+}, \quad (21a)$$

$$DU_0(x) \equiv \partial_z U_2(x, z)|_{z \rightarrow 0^+}, \quad (21b)$$

$$U_b(x) \equiv U_2(x, z)|_{z \rightarrow b^-}, \quad (21c)$$

$$DU_b(x) \equiv \partial_z U_2(x, z)|_{z \rightarrow b^-}, \quad (21d)$$

Hence the field can be found at any desired point once the four unknown functions in Eqs. (21) have been determined. The evaluation of these functions is discussed below.

C. Development of Integral Equations for the Boundary Functions

A set of four integral equations is needed to determine completely the boundary functions. These equations result immediately from application of the continuity equations (10) and (11) to the field equations (20) at the slit boundaries. We find

$$2U_b^-(x) - U_b(x) = \int_{-a}^a \left(\frac{\epsilon_1}{\epsilon_2} \right) G_1(x, b; x', b) DU_b(x') dx' \quad \text{for } |x| < a, \quad (22a)$$

$$U_0(x) = \int_{-a}^a \left(\frac{\epsilon_3}{\epsilon_2} \right) G_3(x, 0; x', 0) DU_0(x') dx' \quad \text{for } |x| < a, \quad (22b)$$

$$\begin{aligned} \frac{1}{2} U_b(x) = & - \int_{-a}^a [G_2(x, b; x', 0) DU_0(x') \\ & - U_0(x') \partial_z G_2(x, b; x', 0)|_{z \rightarrow 0^+}] dx' \\ & + \int_{-a}^a G_2(x, b; x', b) DU_b(x') dx' \quad \text{for } |x| < a, \quad (22c) \end{aligned}$$

$$\begin{aligned} \frac{1}{2} U_0(x) = & \int_{-a}^a [G_2(x, 0; x', b) DU_b(x') \\ & - U_b(x') \partial_z G_2(x, 0; x', b)|_{z \rightarrow b^-}] dx' \\ & - \int_{-a}^a G_2(x, 0; x', 0) DU_0(x') dx' \quad \text{for } |x| < a, \quad (22d) \end{aligned}$$

where

$$U_b^-(x) = \exp[ik_1(x \sin \theta - b \cos \theta)] \quad |\theta| < \frac{\pi}{2}. \quad (23)$$

These coupled equations for the four boundary functions will be solved numerically in the following section.

D. Approximate Solution of the Integral Equations

To demonstrate the technique that will be used to solve the system in Eqs. (22), we consider Eq. (22a). The integral in this expression is first divided into N subintervals of width $2a/N$, each with a central point x_j given by

$$x_j = \frac{2a(j - \frac{1}{2})}{N} - a \quad j = 1, 2, \dots, N. \quad (24)$$

Furthermore, only the field at the midpoint x_k of each subinterval will be considered. Hence we have

$$\begin{aligned} 2U_b^-(x_k) - U_b(x_k) = & \sum_{j=1}^N \left(\frac{\epsilon_1}{\epsilon_2} \right) \int_{C_j} G_1(x_k, b; x', b) DU_b(x') dx' \\ & + \left(\frac{\epsilon_1}{\epsilon_2} \right) \int_{C_k} G_1(x_k, b; x', b) DU_b(x') dx'. \quad (25) \end{aligned}$$

The k th integral is written independently since it contains the point x_k corresponding to the singularity in $G_1(x_k, b; x', b)$ as $x' \rightarrow x_k$.

Equation (25) can be further reduced by applying the first mean value theorem to the $N - 1$ subintervals C_j and the second mean value theorem to the subinterval C_k . This yields

$$\begin{aligned} 2U_b^-(x_k) - U_b(x_k) = & \sum_{j=1}^N \frac{2a}{N} \frac{\epsilon_1}{\epsilon_2} G_1(x_k, b; \xi_j, b) DU_b(\xi_j) \\ & + \frac{\epsilon_1}{\epsilon_2} \left[\int_{C_k} G_1(x_k, b; x', b) dx' \right] DU_b(\xi_k). \quad (26) \end{aligned}$$

The above expression is still exact for some unknown set of N points ξ_j , each within its own corresponding domain C_j . However, an approximation is now introduced to simplify the result. In particular, when the number of subintervals N becomes large, ξ_j can be estimated by the midpoint of each interval:

$$\xi_j \approx x_j \quad (27)$$

so that

$$2U_b^-(x_k) - U_b(x_k) \approx \sum_{j=1}^N s_{kj}^1 DU_b(x_j) \quad k = 1, 2, \dots, N, \quad (28)$$

where

$$s_{kj}^1 = \frac{2a}{N} \frac{\epsilon_1}{\epsilon_2} G_1(x_k, b; x_j, b) \quad \text{for } j \neq k, \quad (29a)$$

$$s_{kk}^1 = \frac{\epsilon_1}{\epsilon_2} \int_{C_k} G_1(x_k, b; x', b) dx' \quad (29b)$$

Equation (28) can be written in matrix form:

$$2\tilde{U}_b^- - \tilde{U}_b = \mathbf{S}^1 \tilde{D} \tilde{U}_b, \quad (30)$$

where the components of the vectors are given by

$$(\tilde{U}_b)_j = U_b^-(x_j) \quad j = 1, 2, \dots, N \quad (31)$$

with similar expressions for $\tilde{U}_b, D\tilde{U}_b$ (and $\tilde{U}_0, D\tilde{U}_0$ later on). The matrix elements are found from the explicit representation of G_1 given in Eq. (16a):

$$s_{kj}^1 = i \frac{a}{N} \frac{\epsilon_1}{\epsilon_2} H_0^{(1)} \left(\frac{2k_1 a}{N} |k - j| \right) \quad \text{for } j \neq k; \quad (32a)$$

$$\begin{aligned} s_{kk}^1 = & i \frac{a}{N} \frac{\epsilon_1}{\epsilon_2} \left\{ H_0^{(1)} \left(\frac{k_1 a}{N} \right) + \frac{\pi}{2} \left[\mathbf{H}_0 \left(\frac{k_1 a}{N} \right) H_1^{(1)} \left(\frac{k_1 a}{N} \right) \right. \right. \\ & \left. \left. - \mathbf{H}_1 \left(\frac{k_1 a}{N} \right) H_0^{(1)} \left(\frac{k_1 a}{N} \right) \right] \right\}. \quad (32b) \end{aligned}$$

The Struve functions \mathbf{H}_0 and \mathbf{H}_1 result from an integra-

tion of the Hankel function $H_0^{(1)}$ about its singularity as outlined by Abramowitz and Stegun.⁷

Application of this same technique to the integral in Eq. (22b) yields a second matrix equation:

$$\bar{U}_0 = \mathbf{S}^{\text{III}} D \bar{U}_0, \quad (33)$$

where

$$s_{kj}^{\text{III}} = i \frac{a}{N} \frac{\epsilon_3}{\epsilon_2} H_0^{(1)} \left(\frac{2k_3 a}{N} |k-j| \right) \quad \text{for } j \neq k, \quad (34a)$$

$$s_{kk}^{\text{III}} = i \frac{a}{N} \frac{\epsilon_3}{\epsilon_2} \left\{ H_0^{(1)} \left(\frac{k_3 a}{N} \right) + \frac{\pi}{2} \left[H_0 \left(\frac{k_3 a}{N} \right) H_1^{(1)} \left(\frac{k_3 a}{N} \right) - H_1 \left(\frac{k_3 a}{N} \right) H_0^{(1)} \left(\frac{k_3 a}{N} \right) \right] \right\}. \quad (34b)$$

Note that \mathbf{S}^{III} , like \mathbf{S}^{I} , has only N independent elements and hence can be readily calculated.

Finally, the integrals in Eqs. (22c) and (22d) can be similarly approximated. After considerable calculation, we obtain

$$\frac{1}{2} \bar{U}_b = -\mathbf{R}^{\text{II}} D \bar{U}_0 + \mathbf{D}^{\text{II}} \bar{U}_0 + \mathbf{S}^{\text{II}} D \bar{U}_b, \quad (35a)$$

$$\frac{1}{2} \bar{U}_0 = -\mathbf{S}^{\text{II}} D \bar{U}_0 + \mathbf{D}^{\text{II}} \bar{U}_b + \mathbf{R}^{\text{II}} D \bar{U}_b, \quad (35b)$$

where

$$r_{kj}^{\text{II}} = \frac{i}{2N\gamma_0} \exp(i\gamma_0 b) + \frac{i}{N} \sum_{m=1}^{\infty} \frac{1}{\gamma_m} T_m^{j,k} \exp(i\gamma_m b), \quad (36a)$$

$$d_{kj}^{\text{II}} = \frac{1}{2N} \exp(i\gamma_0 b) + \frac{1}{N} \sum_{m=1}^{\infty} T_m^{j,k} \exp(i\gamma_m b), \quad (36b)$$

$$s_{kj}^{\text{II}} = \frac{i}{2N\gamma_0} + \frac{i}{N} \sum_{m=1}^{\infty} \frac{1}{\gamma_m} T_m^{j,k}, \quad (36c)$$

$$T_m^{j,k} = \frac{2N}{m\pi} \cos \left[\frac{m\pi(j-1/2)}{N} \right] \cos \left[\frac{m\pi(k-1/2)}{N} \right] \sin \left(\frac{m\pi}{2N} \right). \quad (36d)$$

To improve the convergence in Eqs. (36a)–(36c), the second mean value theorem was used on all N subintervals.

To summarize, the approximation in Eq. (27) has been used to transform the four coupled integral equations in Eqs. (22a)–(22d) into the four coupled matrix equations in Eqs. (30), (33), (35a), and (35b). The remaining goal is to solve this system for the vectors \bar{U}_0 , \bar{U}_b , $D\bar{U}_0$, and $D\bar{U}_b$ which represent the values of the previously unknown boundary functions at N distinct points. Toward this end, \bar{U}_0 and \bar{U}_b can be eliminated from the system to give a single $2N \times 2N$ matrix equation:

$$\mathbf{A} \cdot \bar{\mathbf{B}} = \bar{\mathbf{C}}, \quad (37)$$

where

$$A_{mn} = \begin{cases} (\mathbf{D}^{\text{II}} \mathbf{S}^{\text{III}} - \mathbf{R}^{\text{II}})_{m,n} & \text{for } m, n \in \{1, 2, \dots, N\}, \\ (\mathbf{S}^{\text{II}} + \frac{1}{2} \mathbf{S}^{\text{I}})_{m, n-N} & \text{for } m \in \{1, 2, \dots, N\}, n \in \{N+1, N+2, \dots, 2N\}, \\ (\mathbf{S}^{\text{II}} + \frac{1}{2} \mathbf{S}^{\text{III}})_{m-N, n} & \text{for } m \in \{N+1, N+2, \dots, 2N\}, n \in \{1, 2, \dots, N\}, \\ (\mathbf{D}^{\text{II}} \mathbf{S}^{\text{I}} - \mathbf{R}^{\text{II}})_{m-N, n-N} & \text{for } m, n \in \{N+1, N+2, \dots, 2N\}, \end{cases} \quad (38a)$$

$$B_n = \begin{cases} (D\bar{U}_0)_n & \text{for } n \in \{1, 2, \dots, N\}, \\ (D\bar{U}_b)_{n-N} & \text{for } n \in \{N+1, N+2, \dots, 2N\}, \end{cases} \quad (38e)$$

$$C_n = \begin{cases} (\bar{U}_b)_n & \text{for } n \in \{1, 2, \dots, N\}, \\ (2\mathbf{D}^{\text{II}} \bar{U}_b)_{n-N} & \text{for } n \in \{N+1, N+2, \dots, 2N\}. \end{cases} \quad (38f)$$

$$C_n = \begin{cases} (\bar{U}_b)_n & \text{for } n \in \{1, 2, \dots, N\}, \\ (2\mathbf{D}^{\text{II}} \bar{U}_b)_{n-N} & \text{for } n \in \{N+1, N+2, \dots, 2N\}. \end{cases} \quad (38g)$$

$$C_n = \begin{cases} (\bar{U}_b)_n & \text{for } n \in \{1, 2, \dots, N\}, \\ (2\mathbf{D}^{\text{II}} \bar{U}_b)_{n-N} & \text{for } n \in \{N+1, N+2, \dots, 2N\}. \end{cases} \quad (38h)$$

Since \mathbf{A} and $\bar{\mathbf{C}}$ are composed completely of known elements, the unknowns $D\bar{U}_0$ and $D\bar{U}_b$ can be readily determined. Substitution into Eqs. (35a) and (35b) then determines the remaining unknowns \bar{U}_0 and \bar{U}_b . In other words, by formulating the problem in the language of linear algebra, a discrete solution has been found for the complete diffraction problem. As the number of subdivisions N increases, this discrete solution should approach the true continuous solution.

There are several advantages to the method outlined here. First, the accuracy of the results can be increased without altering the basic algorithm by increasing the number of subintervals. Second, the validity of the solution is not limited to the narrow slit limit. Finally, the electromagnetic fields and energy flux can be determined using the simple numerical approach now to be described.

E. Determination of the Near-Field Energy Flux

When considering a slit as a light source for super-resolution microscopic applications, the degree of collimation of the radiation transmitted into region III is of great significance. Hence the expressions below deal with quantities only in this region, although the same method can be used to find the fields in regions I and II as well.

The first mean value theorem can be applied to the integral expression for the field in Eq. (20b). If the approximation in Eq. (27) is then employed and the Green's function is written in explicit form, we find

$$H(x, z) \approx i \frac{a}{N} \frac{\epsilon_3}{\epsilon_2} \sum_{j=1}^N H_0^{(1)} [k_3 \sqrt{(x-x_j)^2 + z^2}] (DU_0)_j, \quad (39a)$$

where the components $(DU_0)_j$ are found by determining $\bar{\mathbf{B}}$ in the matrix equation (37). From Maxwell's equations we then know

$$E_x(x, z) \approx -\frac{a}{N} \frac{\sqrt{\epsilon_3}}{\epsilon_2} \sum_{j=1}^N \frac{z}{\sqrt{(x-x_j)^2 + z^2}} H_1^{(1)} [k_3 \sqrt{(x-x_j)^2 + z^2}] (DU_0)_j, \quad (39b)$$

$$E_y(x, z) = 0, \quad (39c)$$

$$E_z(x, z) \approx \frac{a}{N} \frac{\sqrt{\epsilon_2}}{\epsilon_2} \sum_{j=1}^N \frac{x - x_j}{\sqrt{(x - x_j)^2 + z^2}} H_1^{(1)}[k_3 \sqrt{(x - x_j)^2 + z^2}] (DU_0)_j. \quad (39d)$$

For field points very close to the screen, the second mean value theorem is needed to avoid the singularities in the Hankel functions.

Finally, it is desirable to present the radiation collimation data in the form of energy flux, since it is the intensity distribution that determines the resolution in near-field microscopy. Hence the time averaged Poynting vector (\mathbf{S}) is the quantity of interest. For time harmonic fields, we find

$$\langle \mathbf{S} \rangle = \frac{c}{16\pi} (\mathbf{E} \times \mathbf{H}^* + \mathbf{E}^* \times \mathbf{H}) = \frac{c}{8\pi} \text{Re}(\mathbf{E} \times \mathbf{H}^*). \quad (40)$$

Furthermore, since the object to be resolved will lie in a plane parallel to the screen containing the slit, we are most interested in the energy flux through such a plane and thus concern ourselves primarily with $\langle S_z \rangle$. Last, the flux should be normalized to the incident flux determined from Eq. (6). This yields

$$\frac{S_z}{S_i} = -\frac{\sqrt{\epsilon_1}}{\cos\theta} \text{Re}(E_x H_y^*). \quad (41)$$

F. Determination of Transmission Coefficients

Although the normalized transmission coefficient for a particular geometry could be calculated by integrating the above expression over the lower edge of the slit, an expression which is more tractable numerically can be obtained by manipulating the integral expression for E_x and H_y . This is demonstrated below.

Integration of the normalized flux over the slit determines the transmission coefficient:

$$T = -\frac{\sqrt{\epsilon_1}}{4a \cos\theta} \int_{-a}^a \left[\lim_{z \rightarrow 0^-} (E_x H_y^* + E_x^* H_y) \right] dx. \quad (42)$$

Using the exact integral forms of E_x and H_y yields

$$T = \frac{i\epsilon_1 \epsilon_3}{4k_1 a \epsilon_2^2 \cos\theta} \lim_{z \rightarrow 0^-} [I_1 - I_2], \quad (43)$$

where

$$I_1 = \int_{-a}^a dx \left\{ \left[\int_{-a}^a \partial_z G_3(x, z; x'', 0) DU_0(x'') dx'' \right] \times \left[\int_{-a}^a G_3^*(x, z; x', 0) DU_0^*(x') dx' \right] \right\}, \quad (44a)$$

$$I_2 = \int_{-a}^a dx \left\{ \left[\int_{-a}^a \partial_z G_3^*(x, z; x'', 0) DU_0^*(x'') dx'' \right] \times \left[\int_{-a}^a G_3(x, z; x', 0) DU_0(x') dx' \right] \right\}. \quad (44b)$$

After several changes in the order of integration, these expressions reduce to

$$T = \frac{i\epsilon_1 \epsilon_3}{4k_1 a \epsilon_2^2 \cos\theta} \int_{-a}^a dx' DU_0(x') \int_{-a}^a dx'' DU_0^*(x'') [I_4 - I_3], \quad (45)$$

where

$$I_3(x', x'') = \lim_{z \rightarrow 0^-} \int_{-a}^a G_3(x, z; x'', 0) \partial_z G_3^*(x, z; x', 0) dx, \quad (46a)$$

$$I_4(x', x'') = \lim_{z \rightarrow 0^-} \int_{-a}^a \partial_z G_3(x, z; x'', 0) G_3^*(x, z; x', 0) dx. \quad (46b)$$

When the explicit form for G_3 is inserted, I_3 and I_4 can be evaluated analytically. It is found that

$$I_3 = \frac{i}{2} H_0^{(1)}(k_3 |x' - x''|), \quad (47a)$$

$$I_4 = -\frac{i}{2} H_0^{(2)}(k_3 |x' - x''|). \quad (47b)$$

Substitution of these expressions into Eq. (45) and subsequent manipulation of DU_0 and DU_0^* lead to the final form of the transmission coefficient:

$$T = \frac{a^2 \epsilon_1 \epsilon_2}{N^2 k_1 a \epsilon_2^2 \cos\theta} \sum_{i=1}^N \sum_{j=1}^N J_0 \left(\frac{2k_3 a}{N} |i - j| \right) \times [\text{Re}[(DU_0)_i] \text{Re}[(DU_0)_j] + \text{Im}[(DU_0)_i] \text{Im}[(DU_0)_j]] \quad (48)$$

where J_0 represents the zeroth-order Bessel function. The elements $(DU_0)_j$ are obtained immediately when the system is solved and J_0 is analytic, so that the transmission coefficient is easily obtained.

III. Numerical Methods

The accuracy and range of validity of this model are limited solely by the number of subdivisions N used in approximating the integral equations as a matrix equation. In particular, G_3 in the analog of Eq. (25) is approx. constant over the intervals C_j , and hence the first mean value theorem can be applied only if the argument of the Hankel function in G_3 is approximately constant. Hence, from Eqs. (17), we must have

$$z > \frac{2a}{N} \quad (49)$$

for the approximations to be valid. Following the example of Neerhoff and Mur, $N = 30$ was used to evaluate our boundary functions, so that the results could be applied to find the energy flux at distances $> 1/30$ of the slit width beyond the screen. The resulting 60×60 matrix equations were solved using Gaussian elimination. The solution was checked for numerical accuracy by backsubstitution into the matrix equation and was found to yield differences in the components of C of less than one part in 10^5 .

IV. Comparison of Transmission Coefficients

The first objective of this study was to check the consistency of the results by comparing the transmission coefficients determined from the integral approach of Neerhoff and Mur with those obtained by the method of Harrington and Auckland. Toward this end, Eq. (48) was used to calculate T for four different slit widths and a variety of screen thicknesses. The results are shown in Fig. 4.

From this figure, it is seen that the transmission resonances of $\lambda/2$ periodicity predicted by Harrington and Auckland are reproduced. Furthermore, the resonance positions are very similar, and the peaks heights are in agreement with the expression

$$T \approx \frac{1}{ka} \text{ at resonance} \quad (50)$$

developed by Harrington and Auckland in the narrow slit limit. In short, the excellent agreement between these two disparate methods lends confidence to the validity of our results.

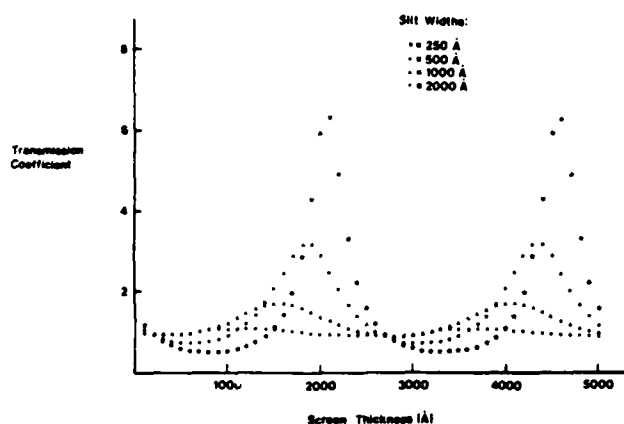


Fig. 4. Transmission coefficients for $\lambda = 5000\text{-}\text{\AA}$ radiation as a function of screen thickness for slits of $\lambda/2.5$, $\lambda/5$, $\lambda/10$, and $\lambda/20$ widths.

V. Results and Implications

A. Near-Field Scanning Optical Microscopy (NSOM)

To determine the degree of collimation within the near field, the boundary functions corresponding to the initial resonant thicknesses of Fig. 4 were used to calculate the energy flux in planes parallel to the screen. The results are shown in Figs. 5 for four different slit widths ($\lambda/2.5$ – $\lambda/20$). From these curves, the full width at half-maximum (FWHM) of the energy flux perpendicular to the screen was determined as a function of the distance from the screen. These results are in Fig. 6.

From the data in Figs. 5 and 6, it is possible to estimate the feasibility of near-field microscopy at optical wavelengths. First, we note that the outward traveling radiation is collimated to exactly the slit width at the edge of the screen. This is a direct consequence of the perfect conductivity assumption but is likely to hold in a realistic situation involving thin metal films of sufficient opacity. Hence the basic concept of superresolution microscopy remains valid: the light passing through an aperture in an opaque screen can be used to define a subwavelength light source, which can then be used to generate an image by scanning.

Further analyses of Figs. 5 and 6 indicate the practical difficulties inherent in near-field microscopy due to the divergence of the radiation past the slit. As an approximate criterion, the FWHM of the radiation distribution is no more than 20% greater than the geometric projection of the slit at a distance of approximately half the slit width. In the visible regime ($\lambda \approx$

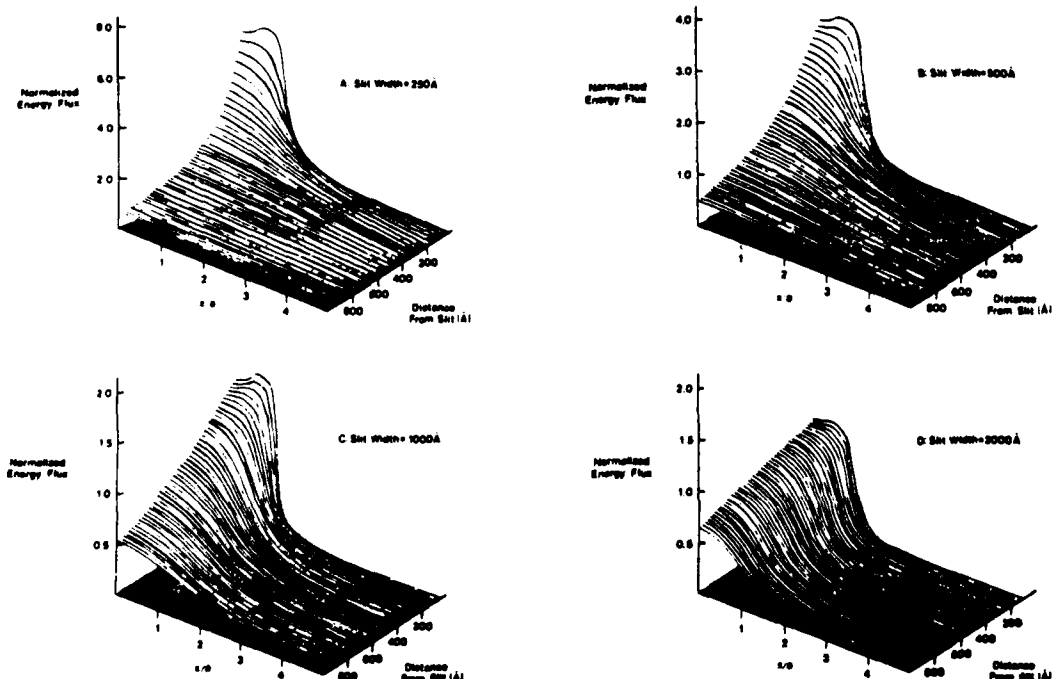


Fig. 5. Distributions of S_z , the component of the energy flux normal to the screen, transmitted by slits of width (A) $\lambda/20$; (B) $\lambda/10$; (C) $\lambda/5$; (D) $\lambda/2.5$ for $\lambda = 5000\text{-}\text{\AA}$ radiation.

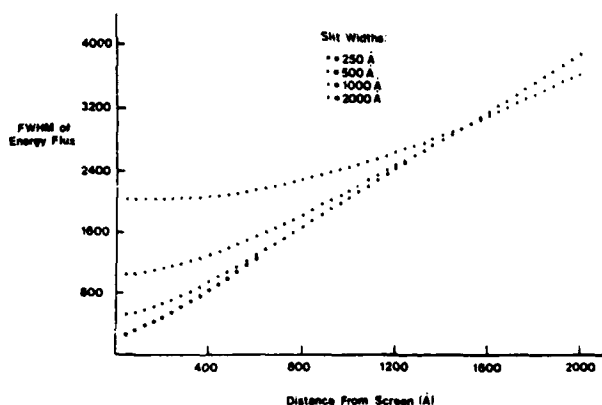


Fig. 6. Rate of spreading of $\lambda = 5000\text{-}\text{\AA}$ radiation past the screen as determined by the FWHM of S_x for slits of $\lambda/2.5$, $\lambda/5$, $\lambda/10$, and $\lambda/20$ widths.

$5000\text{ }\text{\AA}$), this implies that an aperture must be placed within $200\text{ }\text{\AA}$ relative to a surface to obtain an image with $\approx 500\text{-}\text{\AA}$ resolution. If we wish changes in the detected light intensity to be due to variations in optical properties of the sample, the sharp decrease in the peak flux as a function of distance places a further constraint on the precision of the aperture positioning. When scanning over low-contrast samples such as biological specimens, this suggests that a positioning accuracy of $\approx 20\text{ }\text{\AA}$ must be maintained to achieve $\approx 500\text{-}\text{\AA}$ resolution using visible light.

These conclusions clearly illustrate the technical challenges inherent in extending the microwave results of Ash and Nicholls to the optical regime. However, due to recent developments in micropositioning technology such as seen in the scanning tunneling microscope⁸ and the capacitance microscope,⁹ even the strict requirements of near-field optical microscopy can be met. Indeed, by employing micropositioning technology, we have already developed a prototype microscope, the near-field scanning optical microscope (NSOM).^{10,11} With this instrument we have obtained better than $1000\text{-}\text{\AA}$ resolution using a light source with $\lambda \approx 5000\text{ }\text{\AA}$, thus circumventing the conventional diffraction limit. Fischer¹² and Pohl *et al.*¹³ have also worked on the problem of near-field optical imaging and have similarly concluded that subwavelength resolution is achievable. In addition Massey *et al.*¹⁴ have investigated the IR case, where the positioning requirements are less severe because of the larger wavelengths used.

Although half of the slit width can be used to provide an estimate of the collimation distance, it is also clear from Fig. 6 that, even when the distance is scaled to the slit width, the radiation tends to diverge more rapidly as the width decreases particularly for the smaller widths. Hence the apertures used for NSOM should not be made so small as to prohibit positioning of the sample within the collimated near field. Limits on signal detection capabilities also provide a lower bound to the aperture size. On the other, an upper

bound is provided by the fact that the aperture should be at least as small as the desired resolution.

The existence of transmission resonances as a function of screen thickness leads to the question of what effect the screen thickness has on the spatial distribution of the energy flux. Presumably, the high transmission at resonance occurs when the system efficiently channels radiation from a wide area through the slit. In this case, one might assume that if the energy flow is symmetric about the screen, the radiation should diverge very rapidly past the screen at resonance. Thus the large signal strength associated with resonance could only be obtained at the expense of the resolution of the system. To test this hypothesis, energy flux distribution curves similar to those in Fig. 5 were developed for four slit widths corresponding to the anti-resonance positions in Fig. 4. By comparing the two sets of data it was found that the resonance effect does not influence the collimation. To verify this unexpected result, the FWHM of the energy flux was calculated for the four different slit widths as a function of screen thickness at one particular distance from the screen. It was seen that, except for very small thicknesses, the distribution is indeed independent of thickness. Thus high transmission can be achieved without concurrent loss in resolution. In retrospect, this result is reasonable, since the symmetry of the problem is disrupted by the presence of the initial and reflected fields in addition to the diffracted field on one side [Eq. (4)]. As the thickness changes, the fields U^d and U_3 change only in magnitude, but the field U_1 changes in distribution as well since it involves the sum of U^d with the unchanging fields U^i and U^r . At resonance, the distribution of U_1 leads to channeling of the radiation, but the distribution of U_3 remains unaffected.

B. Subwavelength Photolithography

The near-field collimation phenomenon can also be exploited to produce subwavelength structures via photolithography in the visible or near-UV regime. However, because the collimation range is so short at optical frequencies, the pattern in a mask can be reproduced with high fidelity in photoresist only if the mask is in close proximity to the resist and only if the resist itself is very thin. Again referring to Fig. 6, the mask should be $\sim 200\text{ }\text{\AA}$ or less away from the farthest side of the resist to produce $500\text{-}\text{\AA}$ structures. This may be achievable by suitably thinning conventional resists but should certainly be possible using recently developed Langmuir-Blodgett film technology.¹⁵

This method of superresolution pattern generation has already been demonstrated by Fischer and Zingsheim.¹⁶ Using a conventional resist and a blue light source, they obtained $1000\text{-}\text{\AA}$ resolution, and with a photobleaching dye layer they obtained $500\text{--}700\text{-}\text{\AA}$ resolution. We are currently working to extend these results using sharper masks formed by electron-beam lithography.

The model studied here is more applicable to lithography than to microscopy, since the masks used in the

production of integrated circuits are generally formed from multiple slitlike structures, whereas the apertures used for 2-D NSOM must be approximately round. However, the model is restrictive in that the magnetic field is assumed aligned along the slit. This leads to the existence of propagating modes within the slit (and correspondingly large transmission coefficients), but for other polarizations the modes may be evanescent. Thus, if polarized light is used for sub-wavelength photolithography, the exposure of the resist may depend on the orientation of the mask as well as the sizes of the features incorporated therein. To avoid this problem, unpolarized illumination should be used.

The region between the mask and substrate underlying the resist can also form a 2-D waveguide which supports propagating modes.¹⁷ If monochromatic illumination is used, these modes can produce a series of $\lambda/2$ spaced fringes in the developed resist which are analogous to the transmission resonances shown in Fig. 4. However, if polychromatic illumination is used, the field maxima under the mask should occur at different points, so that the fringes are eliminated by destructive interference. For example, a Xe arc lamp would be preferable to a laser or even to a Hg arc lamp, because it has a smooth broadband output in the visible and near UV.

C. Near-Field Scanning Acoustic Microscopy (NSAM)

The above analysis of the near field is also directly applicable to NSAM. In the acoustic case, the magnitude U of the magnetic field H , is replaced by pressure P . This field still satisfies the Helmholtz equation if the excitation is harmonic:

$$(\nabla^2 + k^2)P = 0; \quad (51)$$

$$k = \sqrt{\rho(\omega/c)}; \quad (52)$$

where ρ is the density of fluid (analogous to the index of refraction). The velocity field u is derivable from P just as the electric field E is from the magnetic field, except that it is longitudinal to the direction of travel rather than transverse to it:

$$u = \frac{i}{\omega\rho} \nabla P. \quad (53)$$

Furthermore, if the assumption of perfect conductivity is replaced by the assumption that the screen is perfectly rigid,

$$\partial_n P = 0 \text{ at the screen.} \quad (54)$$

Comparing Eqs. (51) and (54) with Eqs. (3) and (8) it is seen that P satisfies exactly the same differential equation and boundary conditions as does U . Hence the above numerical solution for the magnetic field immediately yields the pressure in the acoustic case, and results concerning the collimation distance and the feasibility of superresolution imaging remain valid.

NSAM has the potential to extend the resolution of conventional diffraction-limited acoustic microscopy¹⁸ in the same manner that NSOM can extend opti-

cal microscopy. However, NSAM has two additional advantages. First, acoustic microscopy is limited in resolution by attenuation within the medium supporting the wave. Since one could obtain $\lambda/10$ resolution using the near-field technique, the frequency of the incident acoustic wave can be reduced by an order of magnitude with no concurrent loss of resolution. The decibel attenuation, which is proportional to the frequency squared, can thus be reduced by a factor of 100 without loss of resolution if a NSAM system with a $\lambda/10$ aperture is employed. Second, a cylindrical acoustic waveguide, such as an aperture in a thick rigid screen, supports at least one propagating mode no matter how narrow the constriction. Hence attenuation of the signal within the aperture should be small compared to the optical case.

D. Topographical Mapping and Mask Alignment

The rapid decrease in the transmitted intensity past a slit can also be used to advantage in two ways. First, a nondestructive topographical instrument could be constructed by collecting light passed through a slit or aperture and reflected back through the aperture by an object within the near field. As the aperture is scanned over an optically uniform surface, the intensity of the reflected light would represent changes in the aperture to object separation due to variations in the height of the object. Second, this same reflection scheme with a feedback mechanism could be used to position a lithographic mask with respect to a substrate.

The analysis of the near-field diffraction by a slit could be applied to a number of other problems as well ranging from electromagnetic interference between close-packed semiconductor devices to the shielding of an environment from rf noise.

VI. Caveats

The limitations of the above analysis must be considered before the results are used to apply near-field phenomena to experimental situations. First, it should be noted that the slit model was chosen more for its mathematical tractability than its correspondence to reality. For example, the metal films which can be used to form a thin screen have finite conductivities and hence are not completely opaque. This would increase the noise in an NSOM system due to passage of a small fraction of the light in the region away from the aperture. Furthermore, the effective diameter of an aperture would increase, since energy could propagate below the surface of the metal wall forming the aperture.

As a general criterion, the perfect conductivity assumption should remain valid as long as the dimensions of the problem (aperture diameter and screen thickness) exceed the extinction length of the radiation within the metal. For aluminum, this length is $\approx 65 \text{ \AA}$ ¹⁹ in the visible, so that the cases treated in Figs. 4-6 easily fall within the range of validity.

The model considered above is also limited to the situation where the incident magnetic field is aligned

along the slit. For other polarizations, the transmitted intensity may be radically different, but the degree of collimation should be about the same.

In interpreting the results, it should be remembered that the FWHM of the outgoing flux provides only an approximate estimate of the resolution to be expected in a NSOM system. Of additional importance is the sharpness of the distribution below the slit, as is evident in Fig. 5. Using this additional criterion, it is seen that the FWHM probably overstates the resolution and that it may be necessary to place the aperture closer than half the width for the resolution to approach the aperture size.

Another potential problem concerns the effect of the object (for NSOM) or the resist and substrate (for lithography) on the distribution of radiation emanating from an aperture. Clearly, any such objects placed within the near field change the boundary conditions and hence the solution of the entire problem. The most significant changes should occur for the case of conducting surfaces, but in all situations one might assume that the substrate should cause the radiation to spread more rapidly, since the screen and surface can act as a waveguide to funnel radiation away from the aperture.

Although the principle of near-field imaging can be investigated using the infinite slit model studied here, a circular aperture must be used for 2-D imaging in NSOM applications. In terms of the transmitted intensity, this can have significant consequences: the slit in a thick screen acts as a waveguide which can support a propagating mode, whereas a round aperture in a thick screen can support only evanescent modes if the aperture is considerably smaller than a wavelength. Furthermore, there is an additional reduction in transmission due to reflections at the screen which occur even in the simpler case of an infinitely thin screen, and these reflections differ for a round aperture as opposed to an infinite slit.

Despite these differences, the slit model was chosen here for a number of reasons. First, finding the near-field radiation pattern from a round aperture in a conducting screen would entail solving a system of two vector fields in three dimensions instead of a single scalar field in two dimensions. Second, consideration of the optical properties of metals indicates that a screen becomes sufficiently opaque only when the thickness approaches the size of the aperture. Hence in a realistic model it is necessary to generalize the thin screen results to the case of nonzero screen thickness. This generalization is accomplished much more simply for the slit geometry. Finally, the results of the thin screen, circular aperture diffraction problem have been expressed as terms in a series expansion for the fields within the aperture.¹ When used to calculate the near-field distribution of radiation, the truncated series yields results of finite accuracy, even when sophisticated numerical methods are used. In contrast, the slit model developed here can be applied to slits of any width in screens of any thickness and will yield results limited only by the speed and memory of the

computer used. The numerical analysis is itself straightforward, so that the boundary fields for a given set of parameters can be determined within a few minutes using a microcomputer.

Nevertheless, the geometry of an aperture closed in two dimensions has been considered by many researchers. Massey²⁰ studied a square aperture in a thin screen using Fourier optics and considered the feasibility of superresolution microscopy and lithography. The qualitative conclusions of the work concerning the extent of collimation are consistent with the more extensive distribution graphs in Figs. 5 (a)-(d), although the approach used may not be valid in the near field. More recently, Leviatan²¹ determined the distribution of the magnetic field transmitted by a circular aperture in a thin screen using the method of moments. The collimation results were also found to be similar to the slit geometry studied here. The more realistic case of a round aperture in a thick screen has been considered by McDonald,²² although only the degree of coupling between the two sides of the screen was investigated rather than the distribution of radiation in the near field.

The results of McDonald can be used to obtain an approximate estimate of the minimum aperture size which can be used for practical NSOM imaging. The least attenuated mode within a round aperture was found to be the TE_{11} mode, for which the energy decays at a rate of

$$E = E_0 \exp(-2 \times 1.841d/a), \quad (55)$$

where d is the screen thickness and a is the aperture radius. However, the energy decays in the screen at a finite rate as well, which is given by

$$E = E_0 \exp(-d/\delta), \quad (56)$$

where δ is the extinction length in the screen. The metal with the largest opacity in the visible is aluminum for which $\delta = 65 \text{ \AA}$ when $\lambda = 5000 \text{ \AA}$.¹⁹ When the attenuation due to the waveguide effect exceeds the attenuation in the metal, the contrast between the aperture and surrounding screen becomes insufficient for superresolution applications. Hence the minimum aperture diameter is given by

$$2a \approx 4 \times 1.841\delta. \quad (57)$$

For Al, this yields a diameter of $\approx 480 \text{ \AA}$, which explains our choice of a goal of 500 \AA for NSOM imaging. It should be noted that this is a very approximate result, since the finite conductivity of the screen should decrease the waveguide attenuation below the value given in Eq. (55) due to the larger effective aperture size as discussed above.

In a strict sense, the resolution of an NSOM system should indeed be limited to the aperture size, since two or more small structures will not be completely resolved if their separation is less than the aperture diameter. However, it should be possible to determine the position of the edge of a structure larger than the aperture (i.e., determine its position) to considerably less than the aperture size. To accomplish this, the

intensity information obtained when the aperture is partially occluded by the edge would be deconvoluted to find the edge position.

Finally, although it is easiest to understand near-field microscopy in the scenario where the aperture is used to form a subwavelength sized light source, this is by no means the only possible mode for NSOM viewing. In addition, the light transmitted through the sample could be collected by the aperture in the near field. In this arrangement, only light from the region directly below the aperture is detected. Although the slit model suggests that this geometry may yield a lower resolution for a given slit to object separation due to the radiation scooping effect at resonance, the resolution should not be affected in the case of a circular aperture since all modes are evanescent and no resonances occur. Finally, light could be both transmitted by and collected with the aperture, thus forming a reflection NSOM instrument. This system has two principal advantages: even thick opaque samples could be scanned, and the resolution and contrast may be higher than in the transmission modes, since the near-field collimation phenomenon is used to advantage not once but twice.

VII. Conclusions

The energy flux transmitted by an infinite slit in a thick conducting screen has been determined using the method of Neerhoff and Mur. The model is limited only in the number of subdivisions required to solve the resulting integral equations by numerical methods. Transmission coefficients were found to be identical to those calculated by the alternative method of Harrington and Auckland. The flux perpendicular to the screen is indeed collimated to the slit width within the very near field but diverges sufficiently rapidly so that an object must be placed closer than half the slit width to generate an image with a resolution approaching this width. In addition to near-field microscopy, other applications such as subwavelength photolithography were considered. Many physical phenomena which may be associated with the optical near field were discussed qualitatively in conjunction with these applications. Finally, limitations of the slit model were viewed in the context of its application to the design and construction of a practical near-field scanning optical microscope.

The authors wish to thank Yehuda Leviatan for many profitable discussions. This work is supported by U.S. Air Force contract AFOSR-84-0314 and NSF contract ECS-8410304. One of the authors (E.B.) is supported as an IBM Graduate Fellow.

References

1. H. A. Bethe, "Theory of Diffraction by Small Holes," *Phys. Rev.* **66**, 163 (1944).
2. C. M. Butler, Y. Rahmat-Samii, and R. Mittra, "Electromagnetic Penetration Through Apertures in Conducting Surfaces," *IEEE Trans. Antennas Propag.* **AP-26**, 82 (1978).
3. E. A. Ash and G. Nicholls, "Super-Resolution Aperture Scanning Microscope," *Nature London* **237**, 510 (1972).
4. R. F. Harrington and D. T. Auckland, "Electromagnetic Transmission Through Narrow Slots in Thick Conducting Screens," *IEEE Trans. Antennas Propag.* **AP-28**, 616 (1980).
5. F. L. Neerhoff and G. Mur, "Diffraction by a Slit in a Thick Screen," *Appl. Sci. Res.* **28**, 73 (1973).
6. P. M. Morse and H. Feshbach, *Methods of Theoretical Physics* (McGraw-Hill, New York, 1953), pp. 812-818.
7. M. Abramowitz and I. A. Stegun, *Handbook of Mathematical Functions* (Dover, New York, 1970), pp. 480, 496.
8. G. Binnig and H. Rohrer, "Scanning Tunneling Microscopy," *Helv. Phys. Acta* **55**, 726 (1982).
9. J. R. Matey and J. Blanc, "Scanning Capacitance Microscopy," *J. Appl. Phys.* **57**, 1437 (1985).
10. A. Lewis, M. Isaacson, A. Harootunian, and A. Muray, "Development of a 500 Å Spatial Resolution Light Microscope," *Ultramicroscopy* **13**, 227 (1984).
11. E. Betzig, A. Lewis, A. Harootunian, M. Isaacson, and E. Kratschmer, "Near-Field Scanning Optical Microscopy (NSOM): Development and Biophysical Applications," *Biophys. J.* **49**, 269 (1986).
12. U. Ch. Fischer, "Optical Characteristics of 0.1 μm Circular Apertures in a Metal Film as Light Sources for Scanning Ultramicroscopy," *J. Vac. Sci. Technol.* **B3**, 386 (1985).
13. D. W. Pohl, W. Denk, and M. Lanz, "Optical Stethoscopy: Image Recording With Resolution λ/20," *Appl. Phys. Lett.* **44**, 652 (1984).
14. G. A. Massey, J. A. Davis, S. M. Katnik, and E. Omon, "Subwavelength Resolution Far-Infrared Microscopy," *Appl. Opt.* **24**, 1498 (1985).
15. A. Barraud, "Polymerization in Langmuir-Blodgett Films and Resist Applications," *Thin Solid Films* **99**, 317 (1983).
16. U. Ch. Fischer and H. P. Zingsheim, "Submicroscopic Pattern Replication With Visible Light," *J. Vac. Sci. Technol.* **19**, 881 (1981).
17. K. L. Tai, R. G. Vadimsky, C. T. Kemmerer, J. S. Wagner, V. E. Lamberte, and A. G. Timko, "Submicron Optical Lithography Using an Inorganic Resist/Polymer Bilevel Scheme," *J. Vac. Sci. Technol.* **17**(5), 1169 (1980).
18. B. Hadimioglu and C. F. Quate, "Water Acoustic Microscopy at Suboptical Wavelengths," *Appl. Phys. Lett.* **43**, 1006 (1983).
19. J. W. Weaver, C. Krafka, D. W. Lynch, and E. E. Koch, "Optical Properties of Metals," *Phys. Daten* **18-2**, 74 (1981).
20. G. A. Massey, "Microscopy and Pattern Generation With Scanned Evanescent Waves," *Appl. Opt.* **23**, 658 (1984).
21. Y. Leviatan, Israel Institute of Technology; private communication.
22. N. A. McDonald, "Electric and Magnetic Coupling through Small Apertures in Shield Walls of Any Thickness," *IEEE Trans. Microwave Theory Tech.* **MTT-20**, 689 (1972).

Super-resolution fluorescence near-field scanning optical microscopy

A. Harootunian, E. Betzig, M. Isaacson, and A. Lewis

School of Applied and Engineering Physics, Cornell University, Ithaca, New York 14853

(Received 19 May 1986; accepted for publication 16 July 1986)

A one-dimensional near-field scanning optical microscope (NSOM) operating in the fluorescence mode has been demonstrated. NSOM line scans of both metallic edges and fluorescent gratings have been obtained and quantitatively compared to both scanning electron micrographs and conventional optical micrographs of the same structures. The sharpness of the near-field scans indicates resolution of < 100 nm.

Lateral resolution in conventional optical microscopy is limited by diffraction effects. It has long been desirable to develop a nondestructive probe which can operate at atmospheric pressures with a spatial resolution approaching that of scanning electron microscopy. Such a probe would have applicability in diverse areas ranging from the biological sciences to semiconductor technology. Towards this goal, near-field scanning optical microscopy (NSOM), is being developed to provide spatial resolution far exceeding that of diffraction limited systems while still using visible wavelengths.¹⁻⁶ In this letter we demonstrate fluorescence NSOM imaging for the first time. This capability is necessary for producing high contrast, super-resolution images and chemical maps of biological and other fluorescent systems.

In NSOM, light transmitted through a submicron aperture in an opaque screen is used to form a light spot which is then scanned over an object to generate an image. If the aperture is in close proximity to the object to be resolved, i.e., within the near field, then resolution is determined primarily by the size of the aperture rather than the wavelength, λ . Quantitatively the near field can be defined as the distance from a screen wherein the initially collimated radiation emanating from an aperture diverges by less than 20%. We have calculated this distance to be $\lambda/25$ for a $\lambda/10$ aperture.⁷ Therefore, at optical wavelengths it is necessary to reduce vibrations to less than 20 nm to achieve the necessary positioning accuracy. Towards this end a 0.6-m-thick optical honeycomb table with an air mount vibration isolation system was used to eliminate vibrations above a few hertz.

Several different methods have been used in the past to fabricate the submicron apertures needed in near-field microscopy.¹⁻⁶ However, we have developed an inexpensive, rapid, and highly reproducible method for producing such apertures at the tips of metallized glass pipettes. Another advantage of this technique is that these highly tapered pipettes can probe recessed regions of rough surfaces. Apertures with diameters ranging from ≈ 50 nm to ≈ 1000 nm (1μ) were formed from glass micropipettes using a two-stage pulling process. The tip outer diameters were approximately 500 nm for the smaller aperture pipettes. Indeed, tips with outer diameters ≈ 20 nm have been produced for use in microinjection of individual cells.⁸

The exterior surfaces of the pipettes were metallized with 8 nm of chromium followed by 50 nm of aluminum via vacuum deposition. The chromium was used as an adhesive layer between the glass pipette and the 50-nm aluminum

layer. Aluminum was chosen for its high absorption coefficient at optical wavelengths. Scanning electron micrographs of a 100-nm-diam pipette and a 600-nm-diam pipette are compared in Fig. 1.

A schematic of the experimental apparatus is shown in Fig. 2. Movement of the pipette was accomplished on a rough scale by micrometer driven stages. Fine positioning was achieved by stacked piezoelectric transducers (PZT's). The PZT's were calibrated both interferometrically and microscopically. Light was passed through the pipette illuminating the aperture from below. The light transmitted by the aperture was then collected by a 25 power 0.55 numerical aperture (NA) microscope objective and focused on a silicon intensified target (SIT) vidicon detector. Both the intensity of the light transmitted and the position of the pipette could be detected by this detector.

Due to the small distance through which the radiation is collimated after emanating from the aperture, it is necessary to know the vertical position of the pipette to within a few nanometers. Coarse vertical positioning was achieved by optically observing the pipette tip come into focus as it was moved toward the object. A small potential was placed between the pipette and the object to be scanned. The pipette was moved vertically upward in steps of 2 nm until a tunneling current was measured at which time the pipette was within a few nanometers of the object surface. At this point intensity data were collected and the pipette was lowered and moved horizontally 25 nm to the next position by stepping the PZT voltage. Scan rates were limited to < 10 pixels per second.

The sample was illuminated through the pipette using a 100-W tungsten lamp with a maximum intensity, λ_{\max} , at 570 nm for the transmission measurements. A dichroic mir-



FIG. 1. Scanning electron micrographs of metallized pipettes with aperture diameters of ≈ 100 nm and ≈ 600 nm at the tips of the pipettes.

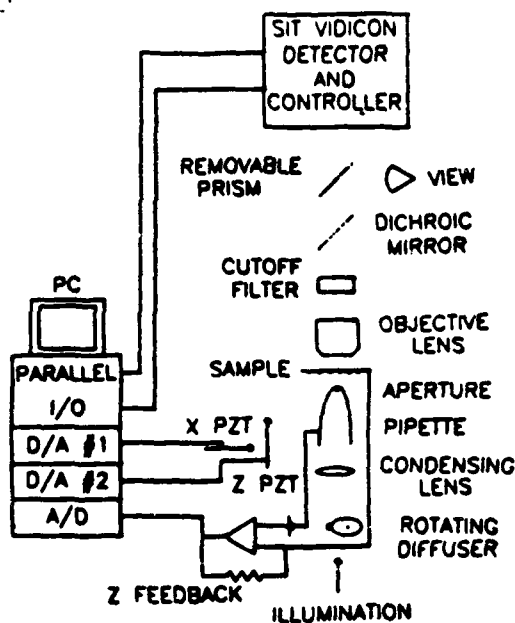


FIG. 2. Schematic of the experiment.

ror was used to cut off the shorter wavelengths. An argon ion laser in all lines visible mode was used for the fluorescence scans. A rotating sand blasted glass window was used to reduce the speckle noise of the laser. A cut-off filter ($\lambda_{1/2} = 580$ nm) was placed between the microscope objective and the detector to block the laser light and to allow the far red ($\lambda_{\max} = 690$ nm) emission to be transmitted to the detector.

Test patterns were made by contact printing a pattern from a mask formed by electron beam lithography.^{5,9} This mask of silicon nitride was placed in contact with a clear glass coverslip and the material to be deposited was then evaporated through the mask and onto the coverslip. For the transmission scans 50 nm of chromium was evaporated whereas 50 nm of 3,4,9,10-perylene-tetracarboxylic dianhydride (Aldrich Chemical Co.) was used for the fluorescence measurements. The samples were then coated with 5 nm of chromium to assure conductivity over the edge or grating. The patterns thus formed had sharp, well characterized features as demonstrated by scanning electron microscopy (SEM). Such test patterns are essential to quantitatively as-

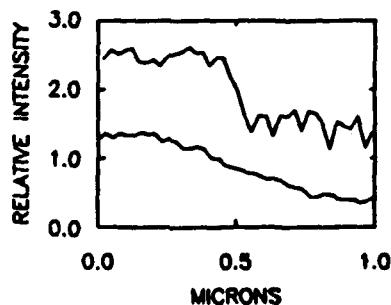


FIG. 3. Low resolution (aperture ≈ 600 nm) and high resolution (aperture ≈ 100 nm) transmission NSOM scans of a 50-nm chromium edge are shown above; $\lambda_{\max} = 570$ nm.

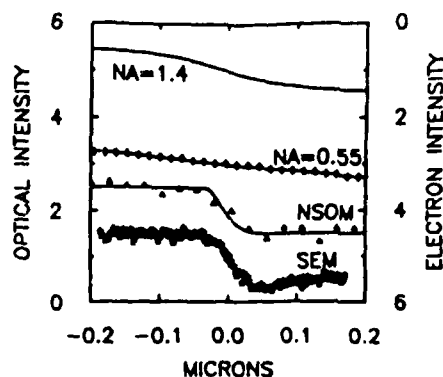


FIG. 4. From bottom to top are shown: a densitometer trace of a scanning electron micrograph of a 50-nm-thick chromium edge; an NSOM scan of the same edge ($\lambda_{\max} = 570$ nm) plotted against a theoretical NSOM curve; a theoretical scanning optical microscope (SOM) scan ($\lambda = 570$ nm, NA = 0.55) plotted with points from an experimental optical micrograph scan of the same 50-nm-thick chrome step taken with $\lambda_{\max} = 570$ nm and NA = 0.55 collection optics used for the NSOM scans, and a theoretical SOM edge scan using a very high (1.4 NA) numerical aperture objective ($\lambda = 570$ nm). All edge scan steps were normalized to an intensity change of unity.

sess the resolution of NSOM in both the transmission and fluorescence modes.

Figure 3 shows a transmission scan over a chromium step for both a 600-nm and a 100-nm aperture. The distance from 12% to 88% transmission scales with aperture size. In Fig. 4 the high resolution NSOM data are compared to a line scan from an electron micrograph of the same edge. The SEM trace is a convolution of the edge profile with the beam profile and the secondary electron emission yield function. The edge profile can be estimated from the micrograph trace to have a width of ≈ 30 nm assuming a beam diameter of 20 nm. This finite width is a result of the contact printing process. The 12–88% point in intensity of the NSOM trace is 60 nm. This is the near-field beam profile convoluted with the 30-nm edge width.

Using these results we can make a quantitative comparison between the SEM and both experimental and theoretical NSOM scans. The theoretical curve through the NSOM data in Fig. 4 was generated by assuming exponential absorption in the chromium step and an intensity transmitted to the detector scaling as the third power of the unoccluded

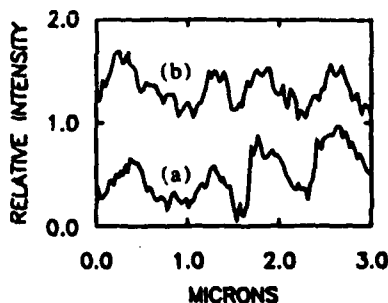


FIG. 5. Fluorescence ($\lambda_{\max} = 690$ nm) NSOM scan of a perylene grating with period 800 nm (a) is shown below a densitometer trace of a SEM scan of the same grating (b). The SEM scan was slightly displaced in a direction parallel to the grating lines relative to the NSOM scan.

aperture area as suggested by Bethe.¹⁰ Also shown in Fig. 4 is a conventional far-field optical line scan obtained from the edge using the same 0.55 NA objective lens as used for the NSOM scans. The solid line passing through these experimental points has been calculated from the theory for a conventional incoherent scanning optical microscope.¹¹ The result of a similar calculation for a 1.4 NA objective is shown at the top of Fig. 4. Thus, one can infer that resolution far exceeding the diffraction limit has been achieved using near-field scanning techniques.

Using the same 100-nm pipettes as were used for the data above we have obtained scans of fluorescent edges and gratings. One such scan of a fluorescent grating of period 800 nm is shown in Fig. 5(a). A densitometer trace of a scanning electron micrograph of the same perylene grating is also shown in Fig. 5(b). The sharpest maximum to minimum change in the fluorescence NSOM image is < 100 nm. Thus, fluorescence NSOM grating scans have been demonstrated with resolution comparable to the aperture diameter used and almost an order of magnitude better than the emission wavelength.

Near-field scanning optical microscopy in both the transmission and fluorescence modes has been demonstrated using a one-dimensional prototype system. Resolution on the order of the aperture size has been demonstrated down to a scale of < 100 nm. The pipette type apertures provide a highly reproducible, easily fabricated, and inexpensive type of submicron aperture. A two-dimensional near-field scan-

ning optical microscope with improved speed, positioning accuracy, vibration isolation, and resolution is under construction. Thus, NSOM shows great promise as a high resolution non-ionizing *in situ* spectral probe.

This work is supported by U.S. Air Force contract AFOSR-84-0314 and NSF contract ECS-8410304. We wish to thank Dr. E. Kratschmer for technical assistance in the grating fabrication. Gratings were fabricated at the National Research and Resource Facility for Submicron Structures (NSF grant ECS-8200312). One of the authors (E. B.) is supported as an IBM Graduate Fellow.

¹A. Lewis, M. Isaacson, A. Muray, and A. Harootunian, *Biophys. J.* **41**, 405a (1983).

²A. Lewis, M. Isaacson, A. Harootunian, and A. Muray, *Ultramicroscopy* **13**, 227 (1984).

³D. W. Pohl, W. Denk, and M. Lanz, *Appl. Phys. Lett.* **44**, 652 (1984).

⁴U. Ch. Fisher, *J. Vac. Sci. Technol. B* **3**, 1498 (1985).

⁵E. Betzig, A. Lewis, A. Harootunian, M. Isaacson, and E. Kratschmer, *Biophys. J.* **49**, 269 (1986).

⁶U. Dürig, D. W. Pohl, and F. Rohner, *J. Appl. Phys.* **59**, 3318 (1986).

⁷E. Betzig, A. Harootunian, A. Lewis, and M. Isaacson, *Appl. Opt.* **25**, 1890 (1986).

⁸K. T. Brown and D. G. Flaming, *Neuroscience* **2**, 813 (1977).

⁹E. Kratschmer and M. Isaacson, *J. Vac. Sci. Technol. B* **4**, 361 (1986).

¹⁰H. A. Bethe, *Phys. Rev.* **66**, 163 (1944).

¹¹T. Wilson and C. Sheppard, *Theory and Practice of Scanning Optical Microscopy* (Academic, London, 1984), p. 34.